

AFRL-RW-EG-TR-2007-7130

KINETICS BASED REACTION MODELING FOR HETEROGENEOUS EXPLOSIVES

J. Keith Clutter

The University of Texas, San Antonio
College of Engineering
6900 North Loop 1604 West
San Antonio, TX 78249



GRANT NO. F08630-02-1-0003

01 JUNE 2007

FINAL REPORT FOR PERIOD JUNE 2002 - JUNE 2007

DISTRIBUTION A: For public release; distribution unlimited. AAC/PA
Approval and Clearance # 11-06-07-630, dated 6 November, 2007

AIR FORCE RESEARCH LABORATORY, MUNITIONS DIRECTORATE

■ Air Force Materiel Command ■ United States Air Force ■ Eglin Air Force Base

NOTICE AND SIGNATURE PAGE

Using Government drawings, specifications, or other data included in this document for any purpose other than Government procurement does not in any way obligate the U.S. Government. The fact that the Government formulated or supplied the drawings, specifications, or other data does not license the holder or any other person or corporation; or convey any rights or permission to manufacture, use, or sell any patented invention that may relate to them.

This report was cleared for public release by the Air Armament Center Public Affairs Office and is available to the general public, including foreign nationals. Copies may be obtained from the Defense Technical Information Center (DTIC) <<http://www.dtic.mil/dtic/index.html>>.

AFRL-RW-EG-TR- 2007-7130 HAS BEEN REVIEWED AND IS APPROVED FOR PUBLICATION IN ACCORDANCE WITH ASSIGNED DISTRIBUTION STATEMENT.

FOR THE DIRECTOR:

// original signed //

Fredric A. Davis, AFRL/RWA

// original signed //

James N. Wilson, AFRL/RWAC

This report is published in the interest of scientific and technical information exchange, and its publication does not constitute the Government's approval or disapproval of its ideas or findings.

REPORT DOCUMENTATION PAGE			Form Approved OMB No. 0704-0188		
Public reporting burden for this collection of information is estimated to average 1 hour per response, including the time for reviewing instructions, searching existing data sources, gathering and maintaining the data needed, and completing and reviewing this collection of information. Send comments regarding this burden estimate or any other aspect of this collection of information, including suggestions for reducing this burden to Department of Defense, Washington Headquarters Services, Directorate for Information Operations and Reports (0704-0188), 1215 Jefferson Davis Highway, Suite 1204, Arlington, VA 22202-4302. Respondents should be aware that notwithstanding any other provision of law, no person shall be subject to any penalty for failing to comply with a collection of information if it does not display a currently valid OMB control number. PLEASE DO NOT RETURN YOUR FORM TO THE ABOVE ADDRESS.					
1. REPORT DATE : 21-06-2007		2. REPORT TYPE: FINAL		3. DATES COVERED: June 2002 – June 2007	
4. TITLE AND SUBTITLE Kinetics Based Reaction Modeling for Heterogeneous Explosives			5a. CONTRACT NUMBER		
			5b. GRANT NUMBER: F08630-02-1-0003		
			5c. PROGRAM ELEMENT NUMBER: 62602F		
6. AUTHOR(S): J. Keith Clutter			5d. PROJECT NUMBER: 2502		
			5e. TASK NUMBER: 07		
			5f. WORK UNIT NUMBER: 35		
7. PERFORMING ORGANIZATION NAME(S) AND ADDRESS(ES) AND ADDRESS(ES) The University of Texas San Antonio College of Engineering 6900 North Loop 1604 West San Antonio, TX 78249			8. PERFORMING ORGANIZATION REPORT NUMBER		
9. SPONSORING / MONITORING AGENCY NAME(S) AND ADDRESS(ES) Air Force Research Laboratory Munitions Directorate AFRL/RWAC Eglin AFB, FL 32542-6810			10. SPONSOR/MONITOR'S ACRONYM(S) AFRL-RW-EG		
			11. SPONSOR/MONITOR'S REPORT NUMBER(S) AFRL-RW-EG-TR-2007-7130		
12. DISTRIBUTION / AVAILABILITY STATEMENT DISTRIBUTION A: For public release; distribution unlimited. AAC/PA Approval and Clearance # 11-06-07-630, dated 6 November, 2007					
13. SUPPLEMENTARY NOTES					
14. ABSTRACT The mechanical and chemical processes that occur in the explosives found in munitions systems are important to the entire life cycle of the system. Examples of these processes are found in the accidental detonation of weapons while in storage or transport, the premature initiation of a warhead during employment, and the destructive output from the system when functioned as designed. The complete range of possible processes encompasses a wide variety of chemical and mechanical phenomena and depending on the scenario, the dominant phenomenon changes. An essential tool for the design and analysis of these systems is a computational model that can predict a range of scenarios. It is such a tool that is the focus of this proposed effort.					
15. SUBJECT TERMS Explosive reaction model, kinetics based reaction model					
16. SECURITY CLASSIFICATION OF:			17. LIMITATION OF ABSTRACT	18. NUMBER OF PAGES	19a. NAME OF RESPONSIBLE PERSON James N. Wilson
a. REPORT UNCLASSIFIED	b. ABSTRACT UNCLASSIFIED	c. THIS PAGE UNCLASSIFIED			19b. TELEPHONE NUMBER (include area code)

1. Introduction

1.1 Problem Definition

Energetic systems are typically designed to function based on the occurrence of a reaction and resulting energy release in a body of energetic material. Solid explosives are typically heterogeneous bodies composed of grains, voids and possibly other materials such as binders. A useful tool in studying energetic systems is computational modeling. Modeling allows for system design while minimizing actual manufacturing and testing. In the case of weapon systems, modeling can also be used to study effectiveness of proposed systems and investigation into off-design scenarios.

Most on-design cases for weapon systems involve a detonation occurring in the energetic material. In terms of modeling a detonation, there are two primary ways to simulate the process. The first is to prescribe the travel and arrival of the detonation which will be referred to here as a prescription method. The second is to solve a rate law equation or equations to simulate the reactions associated with the detonation.

1.2 Modeling Options

The prescription method treats the shock and reaction front composing a detonation as a single entity. There is no attempt to explicitly represent the reaction process. In the simplest of forms, a prescription approach maps out the arrival of the detonation wave to all the locations throughout the energetic material by using the ignition location and the detonation velocity of the material. An example of a more sophisticated prescription model is the Detonation Shock Dynamics (DSD) technique that has been used to successfully simulate various systems ([3]). It is typically used to simulate a formed detonation and the arrival time of the detonation wave to the various parts of the energetic material are mapped out using methodologies that include aspects such as the curvature of the wave. It has been applied for off-detonation cases but has primarily been used for detonations ([19]). The primary limitation of the prescription class of models is they do not offer the universality needed to simulate all possible occurrences in an energetic system.

The rate law approach explicitly models the reaction process within the detonation and the resulting energy release which drives the shock in the detonation. There are a variety of rate law type models. Some are similar to the multi-step, finite-rate temperature based Arrhenius type models commonly used in gas phase combustion. Others employ a simple one-step model with the rate being dependent on the local pressure. These models differ in their formulation but all strive to represent the reaction associated with the detonation as a function of local conditions and not based on an a priori mapping of the explosive body. In this study various rate law models have been tested and each are reviewed in the following sections with results presented.

One objective of the current study is to determine the necessary modeling methodology to capture the various occurrences that are of interest. The purpose for the review in the following section of earlier studies is to determine what sort of modeling frame work is needed to adequately capture all the predominate processes.

1.3 Review of Initiation and Reaction Mechanics

When dealing with detonation modeling, the formulation of all rate law type models begin with an investigation into the processes that initiate and sustain the reactions ([23], [17], [28], [8], [16]). It is universally accepted that the reactions result from "hot spots" that appear in the heterogeneous reactive. The genesis of these areas of localized energy and high temperature is the point of debate and various mechanisms are proposed to be the dominate candidate. The list of phenomena "hot spot" formation is contributed to includes jetting of material from one grain to another, pore collapse, compression of gas within the voids, friction between grains and plastic deformation of the material. The relative importance of the various mechanisms that can cause "hot spot" formation is key in the context of modeling in the sense of the mathematical formulation of the model. It also influences the resolution needs of the model which affects gridding aspects of the computational framework.

[28] provides a short review of the various mechanisms to which "hot spot" formation is attributed. The work of [15] is noted to conclude that gas compression is not a predominant phenomena for hot spot creation when dealing with shock initiation. The role of viscoplastic pore collapse in driving the ignition phase is highlighted as is the role of burning at the external surface of the grains in the growth phase. Modeling is performed using a derivation of the model by [18]. [16] uses a modeling approach that does not explicitly distinguish the various hot spot producing mechanisms but takes a "unifying" approach. This assumes the hot spots can be treated as a single localized heating zone. This approach leverages the fact that in the end, when a model is implemented the finest scale at which differences can be discerned are those equivalent to the mesh or cell space. Therefore, unless resolution is achieved at scales smaller than the grain then in final implementation it is not even possible to distinguish the various hot spot production mechanisms. Therefore a "unified" approach makes sense. The current study follows this same general approach and details are provided later. Here a brief review of initiation mechanisms is conducted with the objective of determining if the modeling framework to be used is adequate to represent the assumptions on which the various rate law models evaluated are based.

It is well accepted that the reaction in the explosive is fundamentally associated with the increase in temperature in the material. However, when dealing with explosives it is hard to isolate the temperature rise associated with the pre-ignition phase from the overall temperature increase during the detonation event. Therefore a review of the response of non-reacting materials

to shocks was conducted. Figure 1 shows a configuration used by [4] to study the effect of particle shape and orientation on copper compaction. Both cylindrical and rectangular particles were insulted with shocks of different strength. Figure 2 shows how changing the shock speed and therefore strength affects the final configuration of the compacted particles. There are clearly noticeable trends as the shock strength is increased. Figure 3 shows that there are material jets created for all impact cases. These jets fill the voids between the particles and penetrate the particles that are downstream from the void. The higher velocities result in deeper penetration and more deformation of all the particles.

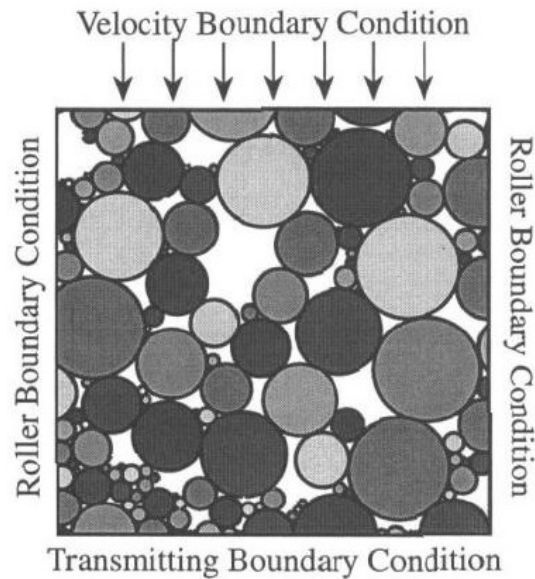


Figure 1. Configuration of copper particles insulted with a shock.

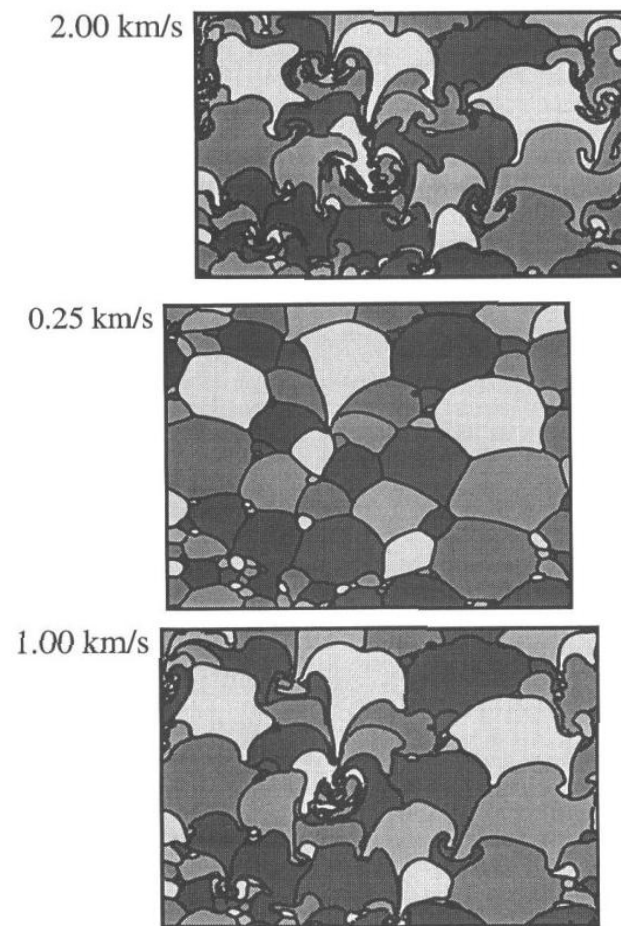


Figure 2. Effect of shock strength on final configuration of the compacted particles.

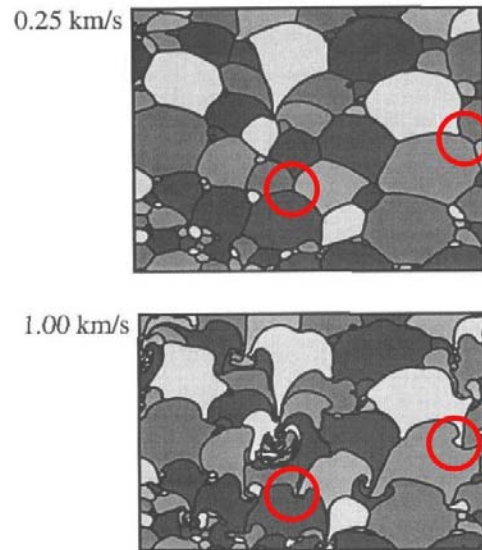


Figure 3. Noticeable trends as shock strength is increased.

The shock strength also affects the temperature rise in the particles which is of particular interest when thinking of the shock compaction process in heterogeneous explosives. For the .25 km/s case the temperature of the interior of the particles is about 350K while the exterior is 380K to 400K. So even at the lower velocity there is heating of the surface due to the impact of the neighboring particles and the deformation of the particle. When the shock velocity is raised to 1 km/s there is a considerably different temperature field produced. Figure 4 shows the variation in temperature along the cut line denoted in the figure. First the interior of the particles are found to rise to about 500K and the temperature at the surfaces of the particles reach up to 1500K and greater.

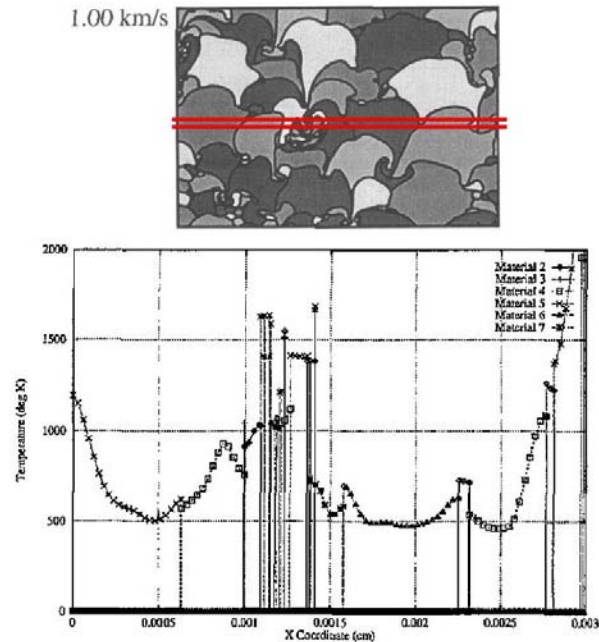


Figure 4. Distribution of temperature across the particle bed for the 1 km/s case.

Benson [4] also investigated the effect of grain shape. The configuration in Figure 5 was insulated with the same range of shock strength as the circular particles. The grain shape is found to affect the load path of the stress as well as the jetting of the material as evident in Figure 6. The range of temperatures resulting from the compaction process are the same as the cylindrical particle cases. Peaks again are associated with material jetting and plastic flow and aligned particles act as a single particle with heating along the boundary of the grouping as evident in Figure 7. Both the cylindrical and rectangular particles show that deformations and heating are localized at the surface of the particles. Furthermore the heating is non-uniform.

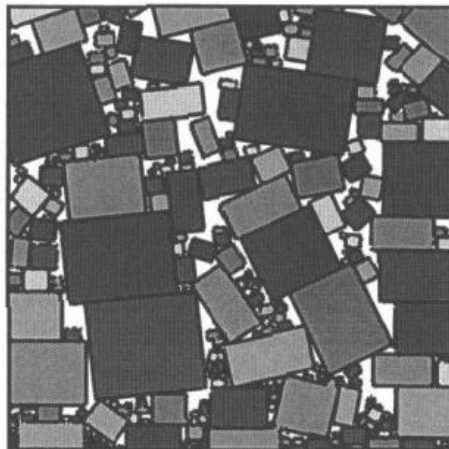


Figure 5. Orientation of rectangular particles in compaction study.

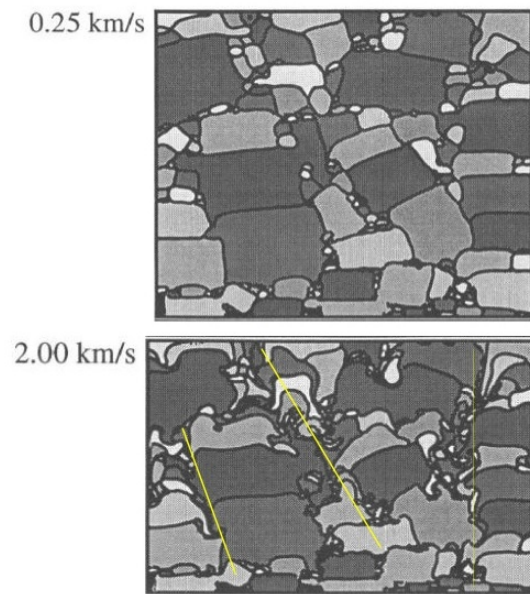
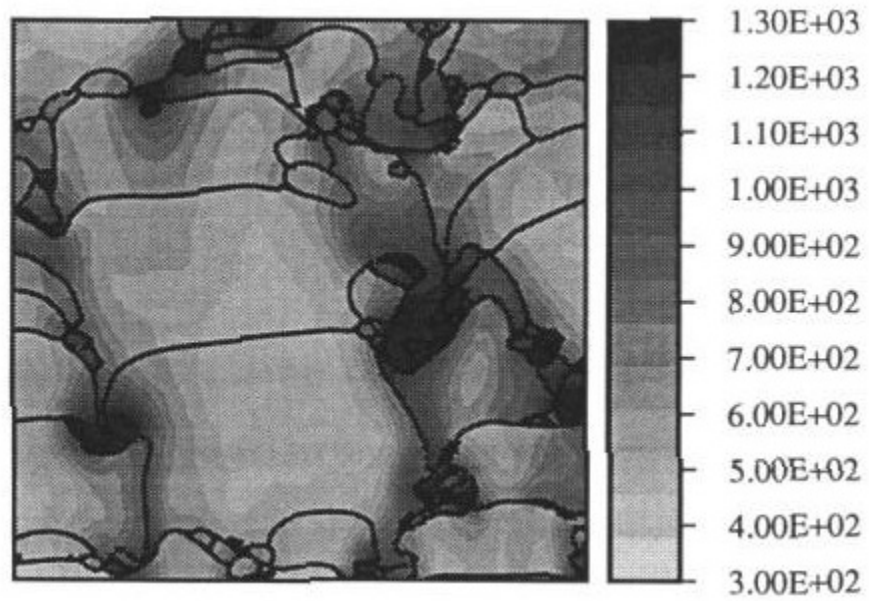


Figure 6. Jetting of material and stress paths in the case of rectangular particles.



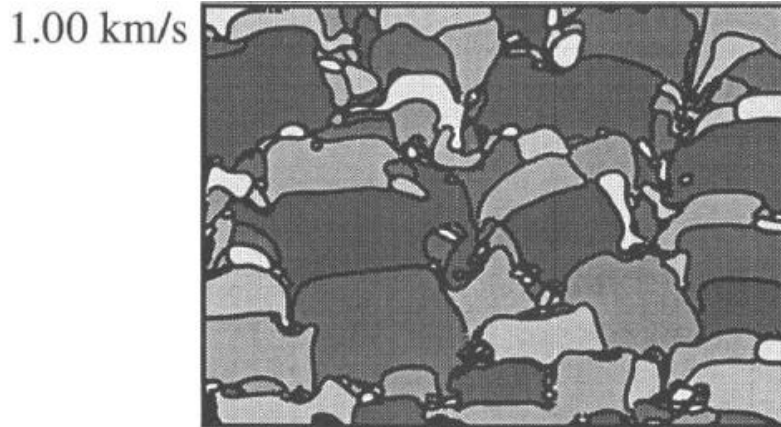


Figure 7. Heating pattern for the 1 km/s case for rectangular particles.

Williamson [39] showed that energy deposition during the compaction of particles is non-uniform. For circular particles undergoing large plastic deformation the frictional heating is small. And due to the short compaction times heat conduction and radiation are negligible. Using the configuration of Figure 8 Williamson [39] determined the effect of shock strength on the final compaction of the particles and associated heating. Figure 9 shows the impact velocity affects the jetting of the material into neighboring particles and influences the local deformation. Impact regions are oriented with the interstitial closures. Figure 10 shows the change in heating through the main body of each particle as the strength of the shock increases. And the heating is found to be elevated at the point of material jetting. The temperature time histories of Figure 11 show the large spikes in temperature occur only at the surface of the particles and correspond to the void closure.

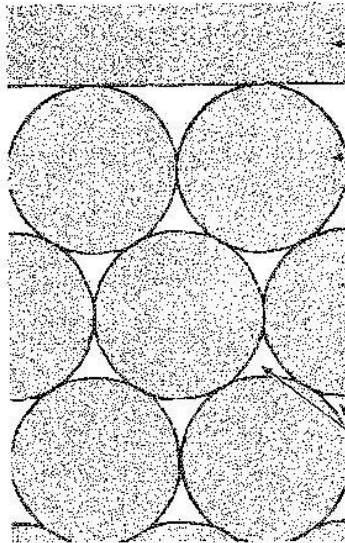


Figure 8. Particle configuration used to evaluate heating during compaction.

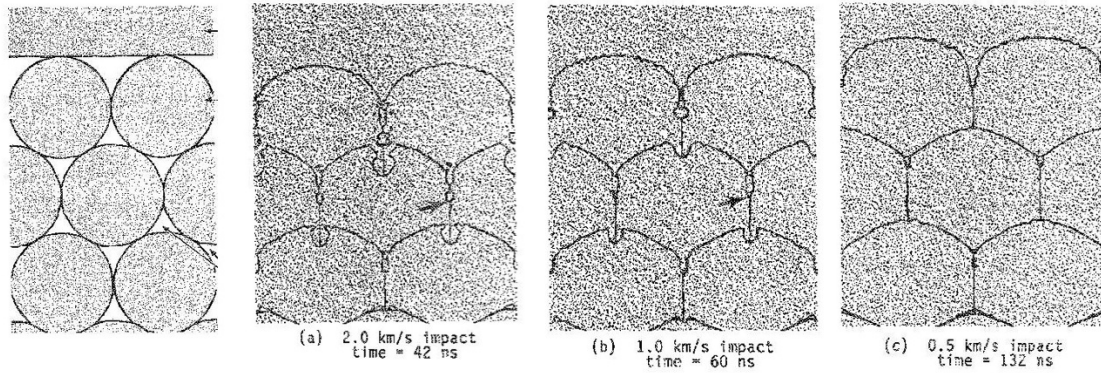


Figure 9. Final particle configuration after compaction for different strength shocks.

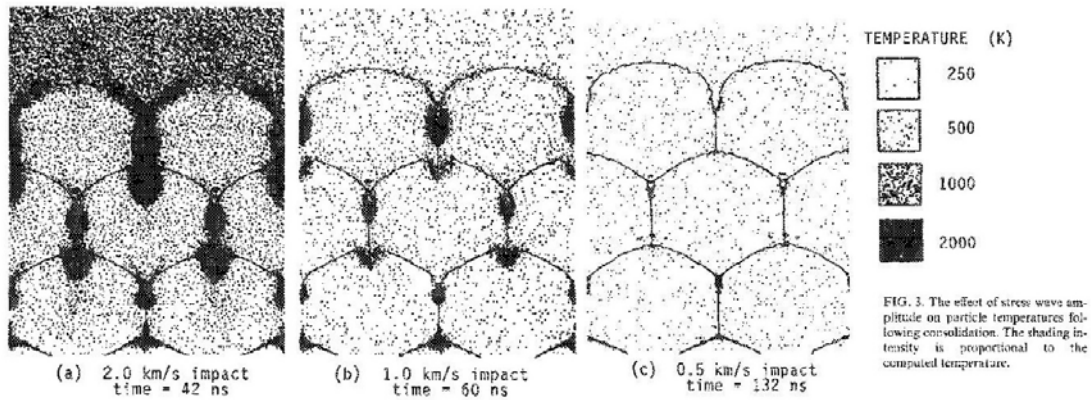


Figure 10. Heating associated with the compaction process.

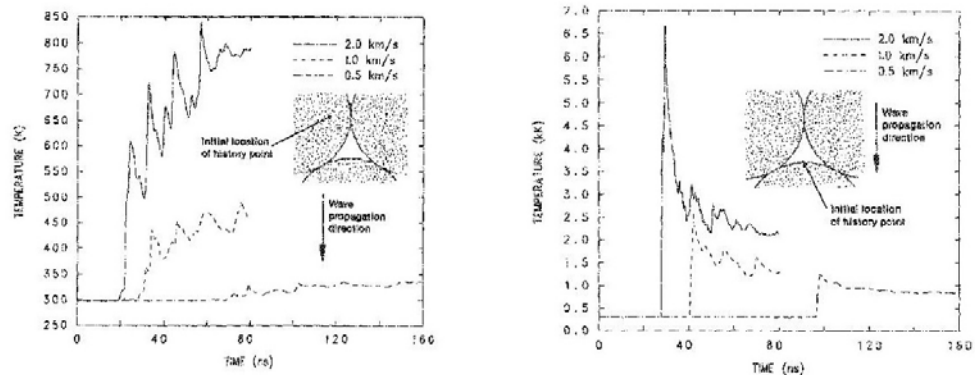


Figure 11. Temperature time histories at a location internal to a particle and at the surface of a particle.

The role of the void is explored by Williamson as well [39]. Simulation results such as that in Figure 12 show the clear role of the void in the production of hot spots in a shocked heterogeneous medium. If the void is minimized by the

insertion of a smaller particle the temperature rises during the shocking are greatly reduced. This matches the data from [4] that shows no significant temperature rise in bodies that are in contact prior to the arrival of the shock. One conclusion from these earlier studies is that one predominate mechanism producing hot spots is the impact of material from one particle (or grain) with another particle (or grain).

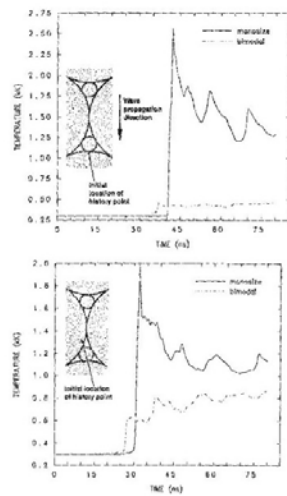


FIG. 7. Comparison of the temperature history at points near the surface of the larger particles, for a hexagonal and monosize particle distribution.

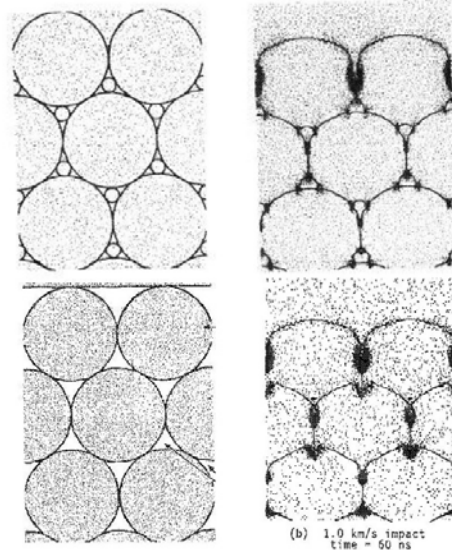


Figure 12. Effect of particle configuration in the compaction and resulting heating.

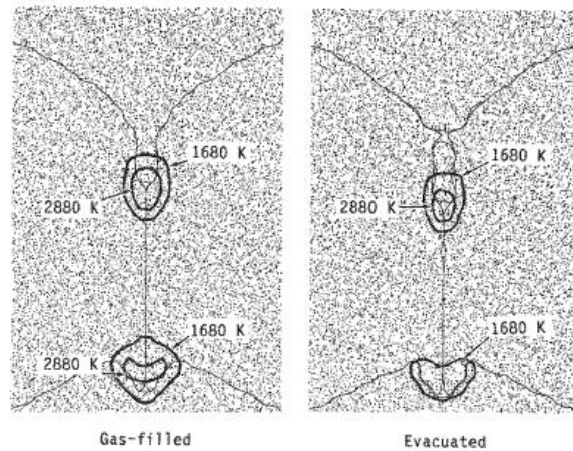


FIG. 11. Temperature contours, comparing the predicted melt zones in the vicinity of initially evacuated and gas-filled voids, at a time just following consolidation of the bottom interstice region.

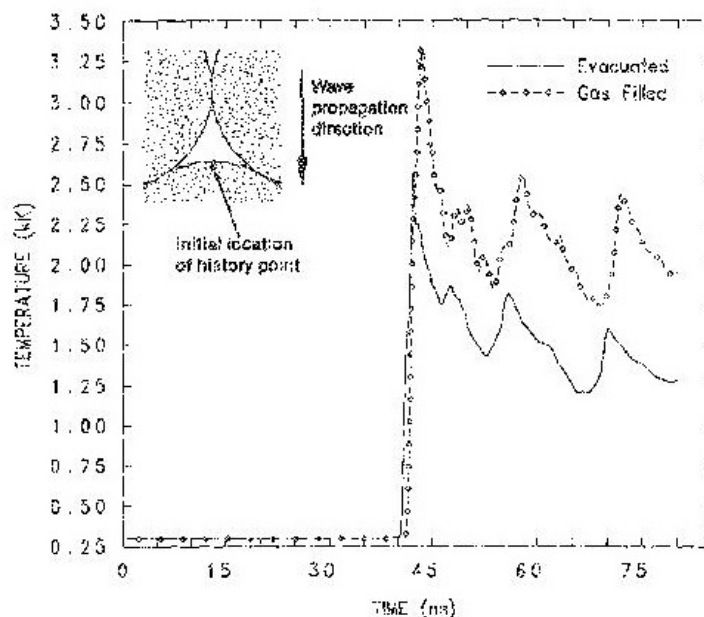


Figure 13. Effect of pore gas in the resulting heating of compacted particles.

As mentioned, the role of the compression of the gas found in the pores in driving the reactions is routinely cited. Some insight into the aspect of the problem can be shed by considering the early work by [39] where the heating of heterogeneous materials were simulated assuming an air filled pore as well as an evacuated pore. Figure 13 shows when the pore is evacuated, the heating of the particle follows a certain pattern due to material compressions and resulting heating. When the pore is filled with air, the pattern is the same but the level of heating is increased. This is due to the fact that with air, and for the same travel of the compressing plate, the grain must be compressed more and therefore the deformation is higher resulting in higher temperatures. Therefore the air is acting as additional mass impacting the grain. For the case of energetic material, this heating can initiate reactions.

There is a difference between the compaction of the inert materials reviewed here versus energetic materials. In the simulations by [39] there is not the potential of reactions occurring between gasified particle material and the pore air. This potential process would be accurately represented by capturing the melting at the grain surface and resulting gasified fuel mixing with pore air and resulting gas phase combustion.

The scenario studied by Williamson [39] was reproduced using the code *cutter* provided to us by the Munitions Directorate. In the simulation a 1-D configuration was considered and three grains of copper were used. The material model for the grains was the Mie-Gruenison model. The grains were compressed as a rate of 1 km/s and 2 km/s. The resulting heating patterns are shown in Figure 14. The trends are similar to those seen in the earlier work by [39] with heating being concentrated at the surface of the grains. The magnitudes are

similar as well.

Simulations using *cutter* were also run for three grains of explosive to simply test the modeling framework. Properties for TNT were used but no reactions were allowed to occur. The predicted compaction and resulting heating patterns early and late in the event can be seen in Figure 15. The results clearly show early in the event, the compaction at the surface of the grains produced localized heating as seen in the inert materials. However, the magnitude of the heating is rather low. Also shown in the figure is the heating history of the grains with each line denoting a different point in time. The heating is found to not remain concentrated at the grain boundaries but is found to be elevated at the interior of the grain. This does not follow the expected behavior for an "inert" material and is most likely due to the inadequacy of the constitutive model used. More on the exact modeling used in this study is provided later.

It is known that various mechanisms can lead to the initiation of reactions in heterogeneous explosive materials such as void collapse and material jetting. It is clear based on the review of micro-scale studies involving inert materials that the hot-spot formation is concentrated at the surface of the grains. And in the configurations studies, the primary heating comes from material of one grain impacting neighboring grains. The impact causes deformation of the grain and associated heating. Earlier studies have supported the conclusion that plastic deformation is the dominate feature of the energy localization [2]. Two observations can be made from these earlier studies. First, to advance alternative modeling options for explosives, appropriate constitutive models are needed for explosive materials. The heating of the grain due to material deformation needs to be accurately resolved. The data also suggests that the dynamics at the smaller scales, i.e. grain-to-grain impact and resulting deformation, may be adequately represented without exactly resolving down to the individual grain. Since heating is focused at the grain surface, a modeling framework that accounts for parameters such as volume fraction of solid and gaseous material and estimates the surface area may be adequate to perform simulations.

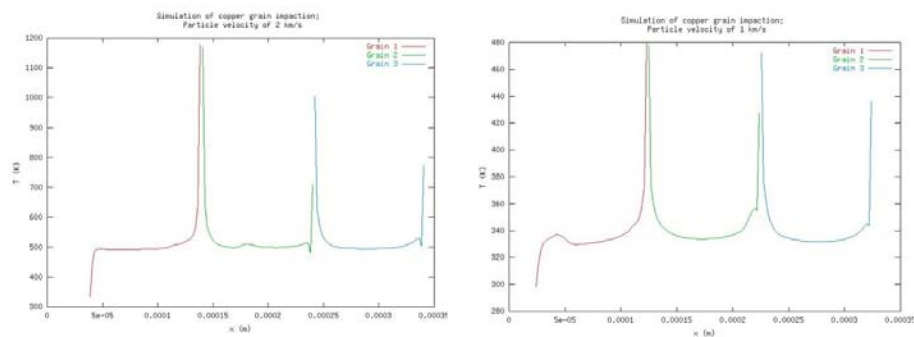


Figure 14. The compaction and resulting heating of copper particles as predicted by *cutter*.

Following the initiation of burning in an energetic material is the growth of the reaction. The growth of reactions in any material are tied to the material properties. It is also tied to the size and shape of the burning front. For the scenarios of interest here the properties are of course those of the solid material and the gases produced from the solids. The size and shape of the burning fronts will be associated with the grain sizes and orientation since the burning originates on the surface of the grain. The evolution of the fronts will depend on the post-compaction configuration of the grains and properties of the material such as the ablation properties of the grains. It is obvious that a micro-scale model with adequate resolution, material properties, and chemical reaction models would accurately predict the growth of the reactions. The question is can a meso-scale model better represent the micro-scale processes than some of the macro-scale models currently used.

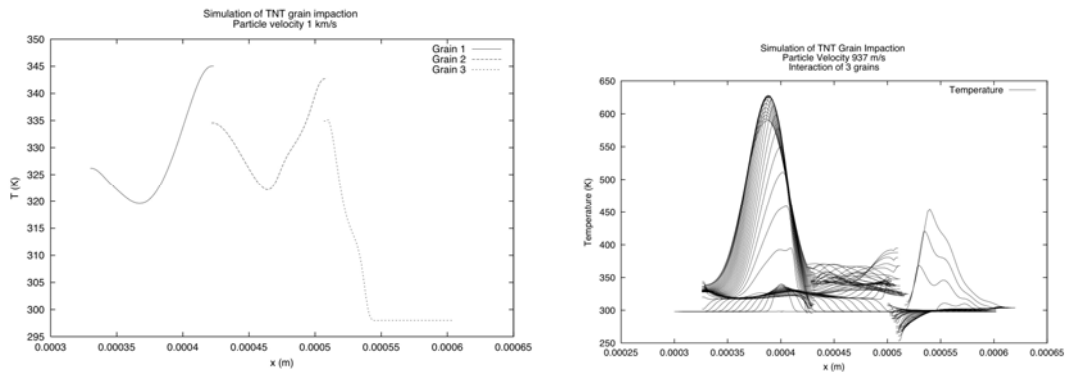


Figure 15. The compaction and resulting heating of TNT particles as predicted by *cutter*.

2. Rate Law Models

Here we will refer to any reaction model that uses local parameters such as pressure, temperature and material concentrations to specify a reaction or burning rate as a rate law model. Figure 16 shows the relative relationship between grains and cell size when using the various models reviewed here.

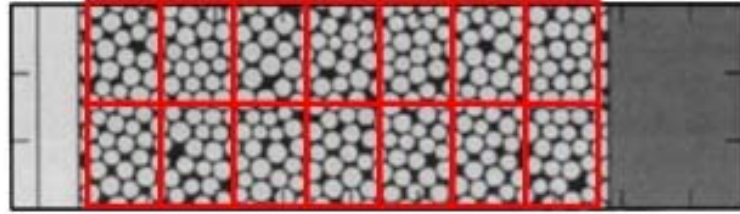


Figure 16. Configuration of multiple grains within a computational cell or element.

2.1 Ignition and Growth

One popular rate law model is the ignition and growth model by [23]. The model uses mixed elements or volumes that contain unreacted explosive and reaction products at equilibrium in terms of pressure. The temperature of the two materials are not in equilibrium and the difference in whether temperature or pressure equilibrium is assumed was quantified in [11]. The model framework uses the Jones-Wilkins-Lee (JWL) equation of state for both materials. The formulation assumes a small fraction of the explosive is ignited by the passing shock in the detonation. This follows the experimental evidence of the localized hot-spot formation. The growth is modeled to be driven by the pressure build up in the material and the surface area of the burning front. Using the assumption of micron-sized spherical burning regions that grow outward, the rate of energy release is modeled using

$$\frac{\partial F}{\partial t} = I(1-F)^x \eta^r + G(1-F)^x F^y P^z \quad (1)$$

$$\eta = V_0/V_1 - 1$$

where F is the fraction of the explosive that has reacted and t is time. The initial specific volume of the explosive is denoted by V_0 and that of the shocked but unreacted explosive by V_1 . The pressure is denoted by P (in megabars) and I , x , r , G , y , and z are constants. The various terms in the equation and associated constants are used to mimic aspects such as the coupling between compression of material, pressure and amount of plastic work involved. The constant G is related to the surface area to volume ratio for the particular material and the P^z

incorporates a pressure dependent laminar burning rate. The term $(1-F)^x F^y$ ensures the rate zeros when there is no more unreacted material and the exponents set the value of F at which the growth of the reaction is maximized.

Results using this model will be presented here which show the model correctly captures the dynamics of a detonation. However, earlier work suggests the model has limited applicability in non-detonation cases [12].

2.2 Hot Spot and Balance

Another rate law model was proposed by [17] where the combustion process is explicitly divided between the hot-spot region and the rest of (or the balance of) the energetic material. The model uses temperature dependent induction times and explicitly tracks intermediate and final material states. A continuum approach is used to represent each element or cell. Studies used to formulate the model in part by studying the fact that the temperature found in hot-spots correlates well with measured induction times in explosives such as HMX. The model framework uses a mixed cell type approach with each component at its particular state. So within a given cell, there is a certain fraction of material that is at the hot-spot state while some is at an intermediate state and the remainder is at the final, post reaction state. If the assumption is made that within a cell, all hot-spots are at the same temperature simulation results capture the peak values in the time history of properties such as material velocities but the actual time history is not correctly resolved. In this mode, the intermediate states are essentially ignored. If the intermediate states are introduced then the simulations are found to correctly capture the time history of the detonation process.

The hot-spot and balance approach is generally the same approach as the ignition and growth in that the different states of the material are represented from unreacted solid energetic material to gaseous detonation products. It is different in that the rate of energy release is temperature based with the form of the rate equation being

$$\dot{f} = (1-f)Z\exp[-\alpha(\theta + \beta f)] \quad (2)$$

where α , β , and Z are constants for the explosive of interest and θ is the local temperature. In the case of both models, empirical parameters are needed to close the models and the models are measured and applied at a continuum level that incorporates both the material grains and pores.

2.3 Temperature Based Kinetics

The models briefly reviewed in the previous two sections were formulated with the main objective being to simulate detonations using local conditions as opposed to using a prescribed type model. The detonation scenario represents one end of the spectrum in terms of time scales of mechanical and thermal

processes. At the other end of the spectrum in terms of time scales is the problem of thermal decomposition of explosive materials. The problem of thermal decomposition during scenarios such as cook-off are routinely modeled using multi-step kinetics models where intermediate products are tracked and the rates are dependent on temperature. It is a goal to eventually model the impact and shock-induced reactions using the same modeling approach [36]. This option will be explored here using a model proposed in [40]. In this earlier study, scaled thermal explosion experiment (STEX) scenarios are modeled using a multi-step, multi-species reaction mechanism.

In the work by [40], a three-step, four-species mechanism for C-4 of the form

$$A \rightarrow B, r_1 = Z_1 \exp(-E_1/RT) \rho_A \quad (3)$$

$$B \rightarrow C, r_2 = Z_2 \exp(-E_2/RT) \rho_B \quad (4)$$

$$C \rightarrow D, r_3 = Z_3 \exp(-E_3/RT) \rho_C^2 \quad (5)$$

where A and B are solid species, and C and D are gases. The parameter r_i is the reaction rate and Z_i is the rate factor and E_i is the activation energy for reaction i . This form is similar to the Arrhenius rate law typically used in gas phase combustion modeling. The parameter ρ_j is the mass fraction of species j .

3. Geometry Representation

There exists a variety of meshing frameworks for use in computational modeling. The main classes are (1) body-fitted curvilinear meshing, (2) unstructured tetrahedral meshing, and (3) Cartesian meshing. All have their pros and cons.

Because the problems of interest here can range in size and configuration it was decided to use the Cartesian meshing approach with the addition of mesh adaptation and refinement. The method employed here uses the basic principles found in the work by [7], [5], and [6]. A short review is provided here but the reader is referred to these earlier works for more details.

Using the Cartesian approach, the domain of interest is defined as any rectangular shape. Also defined is the size of the coarsest grid desired which is referred to as the *Level 0* cells. The cells need not be cubic but larger aspect ratio cells can introduce numerical error depending on the particular flow solver used. Also defined is the number of adaptation levels desired, referred to here as *n_levels*. The two parameters, *Level 0* cell size and *n_levels* will influence both solution accuracy and efficiency. This will depend on the particular problems being solved and benchmark cases will be solved here to determine appropriate settings for the problems of interest.

The Cartesian mesh used here will be adapted as needed to define either geometries or solutions. The particulars of the adaptation will be presented in following sections. Here the fundamentals of the meshing structure are discussed. The domain of interest is decomposed using the specified *Level 0* cells as depicted in Figure 17. If increased resolution is needed these cells are systematically divided into 8 *children*. The requirement for refinement is dependent on a local feature of interest in the geometry or solution. In the current implementation, the discontinuity between neighboring cells is never greater than a 2:1 ratio. This restriction does require that some additional cells be refined other than just those meeting specified criteria. However, it simplifies the flow solver and difference equation solution algorithms and more than adequately accounts for any additional cost.

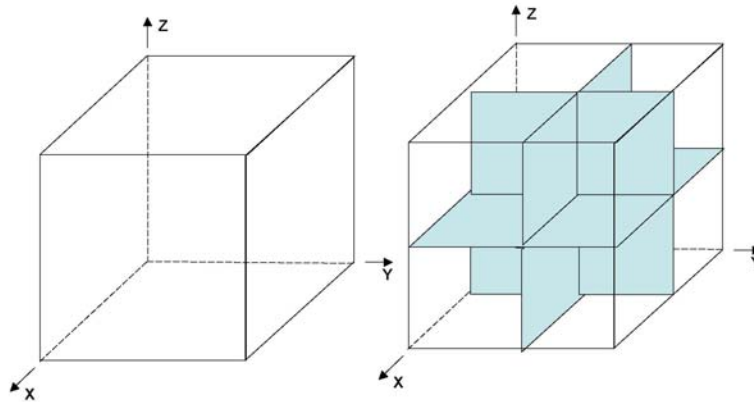


Figure 17. The cell division used when refinement is required. A cell at level n is divided into 8 *children* at level $n+1$.

To facilitate the management of the computational mesh and the solution process, there are some basic grid accounting parameters that need to be associated with each cell. These include the following:

- *level* = level of the cell
- *idiv* = 0 if cell is not divided, = 1 if cell is divided
- *Parent* = pointer to a *parent* cell
- $C2[i][j][k]$ = pointer to *children* cells: $i=0,1$; $j=0,1$; $k=0,1$
- xN = pointer to a *neighboring* cell: $x=L$ (eft), R (ight), B (ottom), T (op), U (nder), O (ver)

The first three parameters are self evident. The third parameter defines the *children* cells if any cell at any level is divided. The pointers are stored in a three-dimensional array making it easy to define algorithms such as flow solvers. Figure 18 shows the definition of the cells and orientation of the numbering. The symbol # denotes that from that vantage point the index could be 0 or 1.

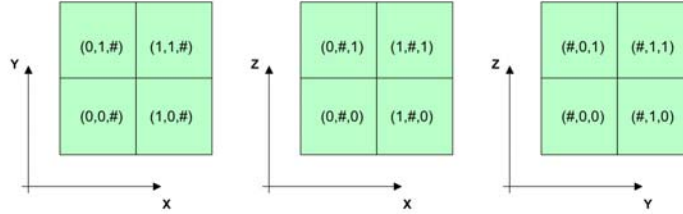


Figure 18. Definition of the children cells.

4. Computational Model

Here the computational model used to simulate the scenarios of interest is detailed. The wave propagation and material transport processes found in the scenarios of interest can be modeled using the Euler equations which can be written in conservative form as

$$\frac{\partial \vec{Q}}{\partial t} + \frac{\partial \vec{F}_i(\vec{Q})}{\partial x_i} = \vec{\Omega}(\vec{Q}) \quad (6)$$

where the subscript i denotes direction and the vectors are

$$\vec{Q} = \begin{bmatrix} \rho \\ \rho u \\ \rho v \\ \rho w \\ \rho E \\ \rho \alpha_1 \\ \vdots \\ \rho \alpha_{NS-1} \end{bmatrix} \quad \vec{F}_i = \begin{bmatrix} \rho u_i \\ \rho u u_i + P \delta_{1i} \\ \rho v u_i + P \delta_{2i} \\ \rho w u_i + P \delta_{3i} \\ \rho u_i H \\ \rho \alpha_1 u_i \\ \vdots \\ \rho \alpha_{NS-1} u_i \end{bmatrix} \quad \vec{\Omega} = \begin{bmatrix} 0 \\ 0 \\ 0 \\ 0 \\ 0 \\ \dot{\omega}_1 \\ \vdots \\ \dot{\omega}_{NS-1} \end{bmatrix} \quad (7)$$

where the subscript i is 1, 2 or 3 respectively to denote the directions x, y or z. The operator $\delta_{\#i}$ works such that the pressure flux functions only on that

component of momentum coinciding with the direction of the flux. The parameters ρ , u , v , and w are respectively the density, x , y , and z components of velocity and P is pressure. The mass fraction of material n is denoted by α_n and ω_n is the source term for that particular material. The parameter NS denotes the number of different materials (or species) involved in the problem and since the overall mass (or density) is conserved then the mass fraction of only $NS-1$ species have to be explicitly tracked since the rules

$$\rho = \sum_{n=1}^{NS} \alpha_n \rho, \quad \sum_{n=1}^{NS} \alpha_n = 1 \quad (8)$$

hold. The source term for each material will be discussed in detail in a following section.

The parameter H represents the total enthalpy ($H = E + P/\rho$) and total energy is represented by the parameter E and is the sum of internal (e) and kinetic ($\frac{1}{2}\bar{u}^2$) energy. For the multi-material problem, the internal energy is a sum of contributions from each species through the equation

$$e = \sum_{n=1}^{NS} \alpha_n e_n \quad (9)$$

and the representation of P_n depends on the nature of material n . For the case of an ideal gas the partial pressure can be represented using

$$P_n = \rho R_u T / M_{w_n} \quad (10)$$

where R_u is the universal gas constant, T is temperature and M_{w_n} is the molecular weight of material n .

For the energetics problems of interest here, materials involved such as the solid explosive and detonation products, require a non-ideal equation of state to be used. Here the Jones-Wilkins-Lee (JWL) equation of state will be used and can be found in two forms, an internal energy dependent form

$$P = A(1 - \omega/R_1 V)e^{-R_1 V} + B(1 - \omega/R_2 V)e^{-R_2 V} + \omega \rho e/V \quad (11)$$

and a temperature dependent form

$$P = Ae^{-R_1 V} + Be^{-R_2 V} + \omega C_v T/V. \quad (12)$$

The parameters A , B , R_1 , R_2 and ω are constants associated with the material, C_v is the average heat capacity and V is the relative volume, ρ_o/ρ , with ρ_o being the initial reference density.

When solving a problem involving multiple materials, the set of equations must be closed assuming either the materials are in equilibrium in terms of pressure or temperature. For the high explosive scenarios, the standard assumption is pressure equilibrium since pressure can equalize much faster than temperature. Using the mass fraction approach and the equilibrium pressure assumption, the contribution from the non-ideal materials to total internal energy can be represented using

$$\rho e_i = VP/\omega_i + \hat{A}_i + \hat{B}_i - E_{o_i} \quad (13)$$

where

$$\begin{aligned} \hat{A}_i &= A_i \left(\frac{1}{R_{1_i}} - \frac{V}{\omega_i} \right) e^{-R_{1_i} V}, \\ \hat{B}_i &= B_i \left(\frac{1}{R_{2_i}} - \frac{V}{\omega_i} \right) e^{-R_{2_i} V}. \end{aligned} \quad (14)$$

The energy component, E_o , is analogous to the heat of formation of the material and since the convention commonly used with the JWL is to define this quantity as a positive number, the value must be subtracted from Equation (13) to produce the correct energy release effect. The pressure of the mixture can be calculated using

$$P = \left[\rho e - \sum_{i=1}^{NS} \alpha_i (\hat{A}_i + \hat{B}_i - E_{o_i}) \right] \left[V \sum_{i=1}^{NS} \alpha_i / \omega_i \right]^{-1} \quad (15)$$

and the temperature of each material can be calculated using

$$T_i = \frac{V}{\omega_i C_{v_i}} \left[P - A_i \exp(-R_{1_i} V) - B_i \exp(-R_{2_i} V) \right] \quad (16)$$

The temperature of the mixture is then calculated using a mass weighted average

$$T = \sum_{i=1}^{NS} \alpha_i T_i \quad (17)$$

The values of the constants are presented later along with the results.

There are a variety of ways to represent the flux terms \vec{F} and two alternative methods were evaluated here. Details of these methods will be presented in a following section. The solution of the source terms is also discussed in a following section.

When considering the solution of the set of equations and the integration of the equations through time, there are also a variety of options with the two main categories being implicit and explicit methods. For the high-speed problems of interest here, the stability advantages of implicit methods which allow for large time steps, are not realized in that small time steps are needed to resolve the phenomena of interest [10]. However, the reaction source term introduces a stiff equation and using implicit methods do have an advantage. Therefore, here a splitting strategy called Strang splitting that has been used successfully in high-speed reacting flows is used. The dependent variables \vec{Q} are advanced from state n to $n+1$ by successively applying the fluid dynamic operator (L_F) and reaction operator (L_Ω) in the order

$$\vec{Q}^{n+1} = L_\Omega^{\Delta t/2} L_F^{\Delta t} L_\Omega^{\Delta t/2} \vec{Q}^n \quad (18)$$

The nature of the fluid dynamics and reaction operators depend on the characteristics of the models being used. For the work here, the fluid dynamics operator used will be explicit while the reaction operator will be explicit or implicit depending on the specifics of the reaction model being used.

5. Numerical Comparisons

5.1 2D Scenario Comparisons

Because the objective here is to move towards simulating energetic systems, the two different numerical flux schemes were also compared within the framework of the adaptive meshing to see if either method demonstrated any noticeable advantages. The test scenario was a simplified, post detonation state mimicking the flyer plate scenario shown in Figure 92. A volume equivalent to the explosive was set to the post detonation state in terms of material, pressure and density as depicted in Figure 93. In the figure are pressure (P), density (ρ), x-velocity (u), y-velocity (v) and mass fraction of the detonation product (DP) plotted along with the dynamic, adapting grid. Also plotted is the adaptation criteria (ε) and the level to which the local grid is resolved (level).

Figure 94 shows the results using the two different methods at a point in time shortly after the initiation of the simulation while Figure 95 compares the results some time later. Both schemes performed well within the adaptive mesh frame work. There were also no significant differences in the results. There is some difference in the contour coloring in the pressure and density plots but this is attributed to the scaling during the plotting and not due to differences in the results.

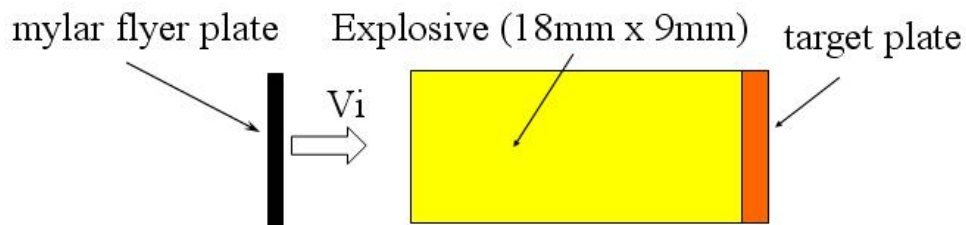


Figure 92. Impact scenario used to compare the numerical flux methods.

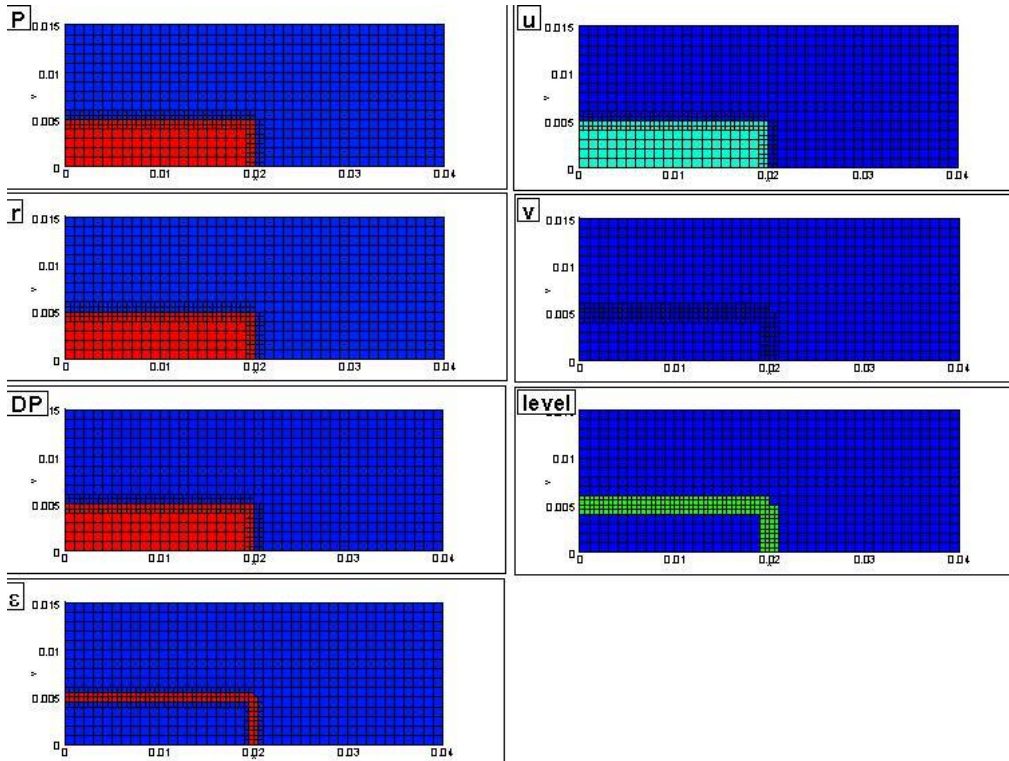


Figure 93. Initial conditions for the 2D test case.

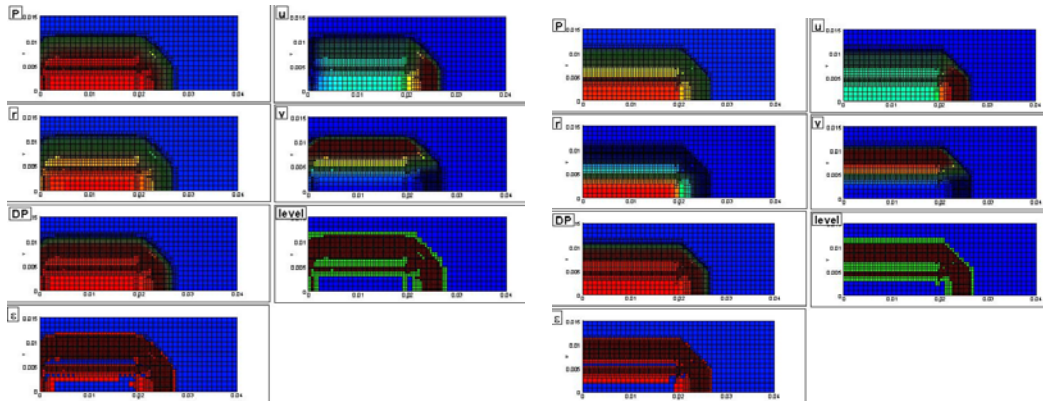


Figure 94. Comparison between the Steger-Warming (left) and AUSM (right) results shortly after initiation of the simulation.

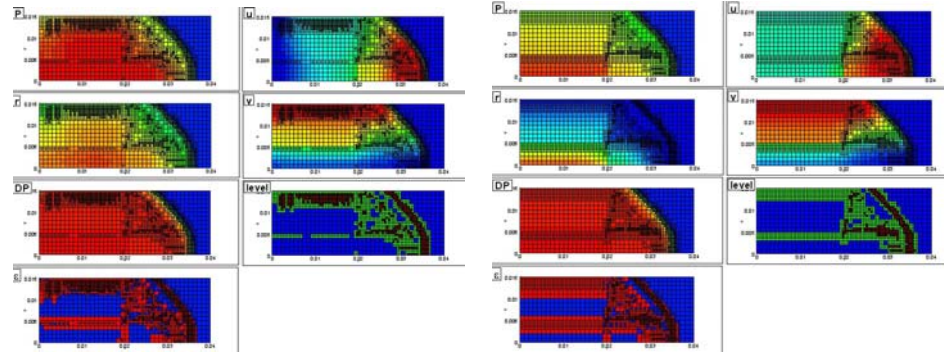


Figure 95. Comparison between the Steger-Warming (left) and AUSM (right) results some time later after initiation of the simulation.

5.2 Findings

In both the 1D and 2D simulations, there are no significant differences found between the results from the Steger-Warming scheme and the AUSM and AUSM+ schemes. There are some boundary issues associated with AUSM but those can be resolved using the approaches mentioned. Because the AUSM schemes do not represent any noticeable advantages we proceeded with using the Steger-Warming scheme because it has demonstrated excellence robustness in previous work.

6. Reaction Source Term Representation

This section contributed by Andrew Staszak and J. Keith Clutter

The governing equations have been presented and the reaction source term is critical to representing the explosion processes. The options in how to model these processes were outlined earlier. All these models constitute a set of equations that have to be solved. Here we evaluate different options to solve the equations. The most complicated model considered here for the energetic materials problem is the multi-step, finite-rate. The reaction models in these systems are very complex and require a great deal of computational effort. When considering chemical reaction simulations, two main factors need to be considered: the speed of the reaction and the characteristic time scale of the flow itself. In applications where the flow field is fast moving a multi-step, finite-rate reaction model must be used to model the combustion process.

Current methods used to solve combustion equation systems have many issues with the extensive computational time needed to compute the chemical kinetics. This computational complexity arises because many of the systems characterized in these types of problems are characterized on a wide range of temporal and spatial scales. This range difference, in most cases, is many orders of magnitude. This range of scales is manifested as “stiffness” in the sets of differential equations. Because of this, many industry models have been reduced to using complex combustion systems only in simple flow problems [9]. To counter these inherent extensive calculations, much of the current effort is centered around mechanism reduction methods, which reduce the number of reactions in the mechanism to a few primary steps. To reduce mechanisms in this manner requires investigative time into the behavior of each reaction in the full mechanism. Reduction methods have been noted to have three major drawbacks [27]:

1. Reductions are specific to a mechanism and require additional human time and labor to develop.
2. Partial-equilibrium and steady-state assumptions can only be applied to specific ranges in composition, pressure, temperature, and time scales. Outside of these ranges results can be poor.
3. Error estimates can only be obtained by comparing the solution of the detailed mechanism to that of the reduced mechanism.

Alternative methods which can reduce computational intensity in existing finite-rate chemistry models would allow for greater ease in the modeling of complex combustion mechanisms in high speed, complex, reacting flows. In this paper, the implementation of numerical derivatives in solving the governing equations is evaluated. The proposed approach is compared to solution methods commonly used in the simulation tools for reactive flows. The three hydrogen-oxygen reaction mechanisms shown in Figure 96, 97, and 98 will be used to

perform the comparisons. This will provide a range of differing complexity to capture any performance dependence on mechanism size.

	Reaction	A_n	B_n	E_{a_n}/Ru
1	$H_2 + O_2 = 2OH$	1.70E+13	0	24233
2	$H + O_2 = OH + O$	1.42E+14	0	8254
3	$H_2 + OH = H + H_2O$	3.16E+07	1.8	1525
4	$O + H_2 = OH + H$	2.07E+14	0	6920
5	$2OH = H_2O + O$	5.50E+13	0	3523
6	$H + OH + M = H_2O + M$	2.21E+22	-2	0
7	$2H + M = H_2 + M$	6.53E+17	-1	0

Figure 96. Seven-step Hydrogen-Oxygen Reaction Mechanism.

	Reaction	A_n	B_n	E_{a_n}/Ru
1	$H_2 + O_2 = HO_2 + H$	1.00E+14	0	28198.8
2	$H + O_2 = OH + O$	2.60E+14	0	8459.64
3	$O + H_2 = OH + H$	1.80E+10	1	4481.6
4	$OH + H_2 = H + H_2O$	2.20E+13	0	2593.28
5	$2OH = O + H_2O$	6.30E+12	0	548.87
6	$H + OH + M = H_2O + M$	2.20E+22	-2	0
7	$2H + M = H_2 + M$	6.34E+17	-1	0
8	$H + O + M = OH + M$	6.00E+16	-0.6	0
9	$H + O_2 + M = HO_2 + M$	2.10E+15	0	-503.55
10	$2O + M = O_2 + M$	6.00E+13	0	-906.39
11	$HO_2 + H = 2OH$	1.40E+14	0	543.83
12	$HO_2 + H = H_2O + O$	1.00E+13	0	543.83
13	$HO_2 + O = O_2 + OH$	1.50E+13	0	478.37
14	$HO_2 + OH = H_2O + O_2$	8.00E+12	0	0
15	$2HO_2 = H_2O_2 + O_2$	2.00E+12	0	0
16	$H + H_2O_2 = H_2 + HO_2$	1.40E+12	0	1812.78
17	$O + H_2O_2 = OH + HO_2$	1.40E+13	0	3222.72
18	$OH + H_2O_2 = H_2O + HO_2$	6.10E+12	0	720.08
19	$H_2O_2 + M = 2OH + M$	1.20E+17	0	22911.53

Figure 97. Nineteen-step Hydrogen-Oxygen Reaction Mechanism.

	Reaction	A_n	B_n	E_{a_n}/R_u
1	$H_2 + O_2 = HO_2 + H$	1.00E+14	0	28198.8
2	$H + O_2 = OH + O$	2.60E+14	0	8459.64
3	$O + H_2 = OH + H$	1.80E+10	1	4481.6
4	$OH + H_2 = H + H_2O$	2.20E+13	0	2593.28
5	$2OH = O + H_2O$	6.30E+12	0	548.87
6	$H + OH + M = H_2O + M$	2.20E+22	-2	0
7	$2H + M = H_2 + M$	6.34E+17	-1	0
8	$H + O + M = OH + M$	6.00E+16	-0.6	0
9	$H + O_2 + M = HO_2 + M$	2.10E+15	0	-503.55
10	$2O + M = O_2 + M$	6.00E+13	0	-906.39
11	$HO_2 + H = 2OH$	1.40E+14	0	543.83
12	$HO_2 + H = H_2O + O$	1.00E+13	0	543.83
13	$HO_2 + O = O_2 + OH$	1.50E+13	0	478.37
14	$HO_2 + OH = H_2O + O_2$	8.00E+12	0	0
15	$2HO_2 = H_2O_2 + O_2$	2.00E+12	0	0
16	$H + H_2O_2 = H_2 + HO_2$	1.40E+12	0	1812.78
17	$O + H_2O_2 = OH + HO_2$	1.40E+13	0	3222.72
18	$OH + H_2O_2 = H_2O + HO_2$	6.10E+12	0	720.08
19	$H_2O_2 + M = 2OH + M$	1.20E+17	0	22911.53
20	$2N + M = N_2 + M$	2.80E+17	-0.75	0
21	$N + O_2 = NO + O$	6.40E+09	1	3172.36
22	$N + NO = N_2 + O$	1.60E+13	0	0
23	$N + OH = NO + H$	6.30E+11	0.5	0
24	$H + NO + M = HNO + M$	5.40E+15	0	-302.13
25	$H + HNO = NO + H_2$	4.80E+12	0	0
26	$O + HNO = NO + OH$	5.00E+11	0.5	0
27	$OH + HNO = NO + H_2O$	3.60E+13	0	0
28	$HO_2 + HNO = NO + H_2O_2$	2.00E+12	0	0
29	$HO_2 + NO = NO_2 + OH$	3.40E+12	0	-130.92
30	$H + NO_2 = NO + OH$	3.50E+14	0	755.33
31	$O + NO_2 = NO + O_2$	1.00E+13	0	302.13
32	$M + NO_2 = NO + O + M$	1.16E+16	0	33234.3

Figure 98. Thirty two – step Hydrogen-Oxygen Reaction Mechanism.

6.1 Governing Equations

The governing equations for the complete propulsion system problem include the Navier-Stokes equations. Because the focus here is on the chemical reaction aspects, the governing equation can be represented in the vector form

$$\frac{\partial}{\partial t} Q = \Omega \quad (19)$$

where only the dependent variables and their source terms remain in the equation. Equation (19) represents the constant density chemical reaction model that will be used in this paper. The terms Q and Ω represent vectors containing

density and terms specific to each species represented in a mechanism. The vector of dependent variables is

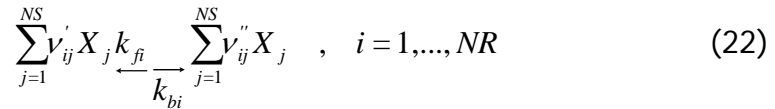
$$Q = [\rho, \rho\alpha_1, \dots, \rho\alpha_{NS-1}]^T \quad (20)$$

where α is the mass fraction of the i th species, and NS is the total number of species in the mechanism. The source terms are represented in the vector

$$\Omega = [0, \dot{\omega}_1, \dots, \dot{\omega}_{NS-1}]^T \quad (21)$$

where the terms are only represented to the NS-1 species since overall mass conservation is maintained. The source terms represent the production rates of each individual species in the mechanism. These terms incorporate both the forward and backward production rates of each species throughout all of the reactions of the mechanism. The solution assumes a mixture of perfect gases and conserves total energy. The specific heat of each species is represented using JANAF data [29].

The chemical model is represented by a reaction mechanism containing any number of reactions (NR) and species (NS). These reactions are in the form



where ν'_{ij} and ν''_{ij} are the stoichiometric coefficients for species j in reaction i , and X_j is the molecular concentration of species j . The forward and backward reaction rates are represented in the terms k_{fi} and k_{bi} for each reaction. The forward reaction rates are calculated using the Arrhenius rate expression

$$k_{fi} = A_i T^{b_i} \exp\left[\frac{-E_{a_i}}{R_u T}\right] \quad (23)$$

where R_u is the Universal Gas Constant. A_i is the pre-exponential factor, b_i is the temperature exponent, and E_{a_i} is the activation energy for the forward reaction and values used can be found in Figures 96, 97, and 98. The backward rates are calculated using the relationship between the equilibrium constant and the forward and backward rates. The production rates of each individual species are calculated through a summation of contributions from each reaction and represented symbolically as

$$\dot{\omega}_j = m w_j \sum_{i=1}^{NR} (\nu''_{ij} - \nu'_{ij}) \cdot \left[k_{fi} \prod_{n=1}^{NS} X_n^{\nu'_{in}} - k_{bi} \prod_{n=1}^{NS} X_n^{\nu''_{in}} \right] \quad (24)$$

Where mw_j represents the molecular weight of the species.

The governing equations result in a system of equations that must be integrated in time. When coupled with the fluid dynamic terms the time step is typically set by the CFL condition associated with the flow. The restrictions from the fluid aspects of the problem are typically less restrictive than the reaction aspects. A common approach is the use of a split operator method that allows different solutions methods to be used for the fluid dynamic operation versus the reaction operations [10]. This allows the overall time step to be set based on parameters of the study. If it is set such that the restrictions associated with the fluid dynamics will define the time step between state n and $n+1$, then the reaction operator is used to advance the chemical reactions from one state to the next. The focus here is on numerical methods used for the reaction operator. The reaction system of equations can be solved in a variety of means and one of the simplest options is the use of explicit methods. Explicit schemes allow for the dependent variables to be directly computed in terms of known quantities. In the reaction model, the partial derivative of the dependent variables, Q , with respect to time can be found using a first order upwind difference operator [21]. In difference form, the system of equations is

$$Q^{n+1} = Q^n + \Omega^n \Delta t \quad (25)$$

where the superscript denotes the time level at which the vector of variables is represented. The Δt is chosen based on the reaction mechanism that is being modeled. Although explicit schemes are simple, they have very low stability and can easily produce non-physical solutions. Because of this, careful attention must be paid when choosing a step size.

Another option is the use of a Runge-Kutta scheme. This approach is an attempt to benefit from the simplicity of explicit methods while decreasing computational time. Here the Fourth-Order Runge-Kutta will be used. The reaction model is represented as a first order differential with initial values

$$\frac{\partial Q}{\partial t} = \Omega(t, \rho\alpha), \quad \rho\alpha(t_0) = \rho\alpha^0 \quad (26)$$

where the initial values would be Q^n . By formal integration of the derivative and applying Euler's algorithm, the fourth-order method can be written as [32]

$$\begin{aligned}
k_1 &= hf(t^n, \rho\alpha^n) \\
k_2 &= hf\left(t^n + \frac{h}{2}, \rho\alpha^n + \frac{k_1}{2}\right) \\
k_3 &= hf\left(t^n + \frac{h}{2}, \rho\alpha^n + \frac{k_2}{2}\right) \\
k_4 &= hf(t^n + h, \rho\alpha^n + k_3) \\
\rho\alpha^{n+1} &= \rho\alpha^n + \frac{k_1}{6} + \frac{k_2}{3} + \frac{k_3}{3} + \frac{k_4}{6} + O(h^5)
\end{aligned} \tag{27}$$

This method requires the evaluation of the source terms in the governing equations four times for each time step. Thus, the value at the next time step is found using the present value plus a weighted average of the slopes at several points. The goal of the Fourth-Order Runge-Kutta method is to increase the size of time step that can be taken compared to the generic explicit method.

Another option is to solve the set of equations using an implicit approach. Such an approach helps address issues such as stability in the solution process and numerical restrictions associated with the time steps. The difference equations that are actually solved come from the linearization of the chemical reaction source term

$$\Omega^{n+1} = \Omega^n + (A)^n \Delta Q \tag{28}$$

where

$$A = \frac{d\Omega}{dQ} \tag{29}$$

is the Jacobian matrix. Substituting the expansion into the governing equations, the system becomes

$$\left[I - A^n \frac{\Delta t}{2} \right] (Q^{n+1} - Q^n) = \Omega^n \Delta t \tag{30}$$

where I is the identity matrix and represents a system of coupled linear equations in the form of $Ax = b$.

Even when using the implicit method there remains a variety of options that finalize the solution approach. One option is the solution of the equation set and here the LU Decomposition method will be used. Another option is the formulation of the Jacobian matrix. This choice itself can affect the computational time required to perform a simulation. One approach that can greatly reduce run time is to determine the Jacobian analytically [10]. However, this approach requires preprocessing using other software tools rather than just the tool to be used for the reaction simulation. Furthermore this preprocessing is

required for each reaction scenario to be considered. Therefore for the current study this approach will not be used.

The first option to establishing the Jacobian is a generic approach where the computational routine uses a set of do loops with the parameters being set by an input file. Such an approach does not require extensive preprocessing before executing a simulation but only reading a simple file that defines the mechanism such as Figures 96, 97, and 98. This approach will be one of the methods evaluated here.

Algorithms utilizing do loops can be computationally expensive because of the many looping functions. To overcome this limitation, an alternative approach using numerical derivatives will be evaluated. By calculating the Jacobian numerically, only a single looping function is required as opposed to several embedded functions used in the general implicit approach. A study by Orkwis and Vanden, which compared the use of numerical derivatives and analytic representation of the Jacobian terms in the full Navier-Stokes equations, found that numerical derivatives can be used to accurately represent the terms of the Jacobian [31]. Assuming that one has the function , the definition of its derivative is

$$\frac{df}{dx} = f'(x) = \lim_{h \rightarrow 0} \frac{f(x+h) - f(x)}{h}. \quad (31)$$

Using the form above, the derivatives of each source term that composes the Jacobian can be represented as

$$\frac{d\omega_i}{\partial \rho \alpha_j} = \frac{\omega_i(\rho \alpha_j + h) - \omega_i(\rho \alpha_j)}{h} \quad (32)$$

where i and j represent each species in the mechanism and h a deviation in the concentration of species j. Because the source term at state n has to be calculated for any method used to solve the reaction equations, the numerical derivative approach requires only an additional calculation which can be done within a single looping function.

The numerical derivatives contain two sources of error, truncation error found in any difference equation and roundoff error. The roundoff error is inherent in any computer model due to machine accuracy. If the size of h is outside the precision of the computer or programming environment, the machine's floating point representation may not accurately represent the effect of h. The worst case of this is where the value of h is lost in rounding and the resulting derivative becomes zero or undefined.

6.2 Results

As a starting point for the analysis, initial conditions were chosen to be representative of temperatures and pressures that would be found in a high speed reacting flow such as a high explosive process. For this, a temperature of 1600 K and a pressure of 1125 kPa will be used as a baseline for comparison. Each scheme was run using a constant time step of 1E-9 seconds and run for the three reaction mechanisms. This small value was chosen to ensure stability for all methods.

Figures 99, 100, and 101 show plots of temperature versus time for each method and the various reaction mechanism. The temperature histories produced by the general explicit, Runge-Kutta, and numerical derivative schemes are almost identical but the history of the general implicit scheme differs. Although the general implicit method deviates, it reaches the same steady state conditions as the explicit methods and the numerical derivative method. The deviation of the generic implicit method can be attributed to roundoff error accumulated in the calculations which has been found in other studies [31]. The 19-step and 32-step mechanisms produce similar results but as the mechanism becomes more complex the difference between the general explicit results and the others becomes smaller.

Another obvious result is the difference in the predicted heat release as the difference mechanisms are chosen. The 19-step and 32-step mechanisms results are somewhat similar but the 7-step is considerably different. This reinforces the point that when a reduced mechanism is used fundamentally different predictions can result. This is particularly true if the reduction was meant for a particular operational scenario but the problem of interest falls outside this scenario. It further emphasizes the need to have better numerical techniques that allow for more complex mechanisms to be used, particularly when addressing problems where the chemical processes are not well defined.

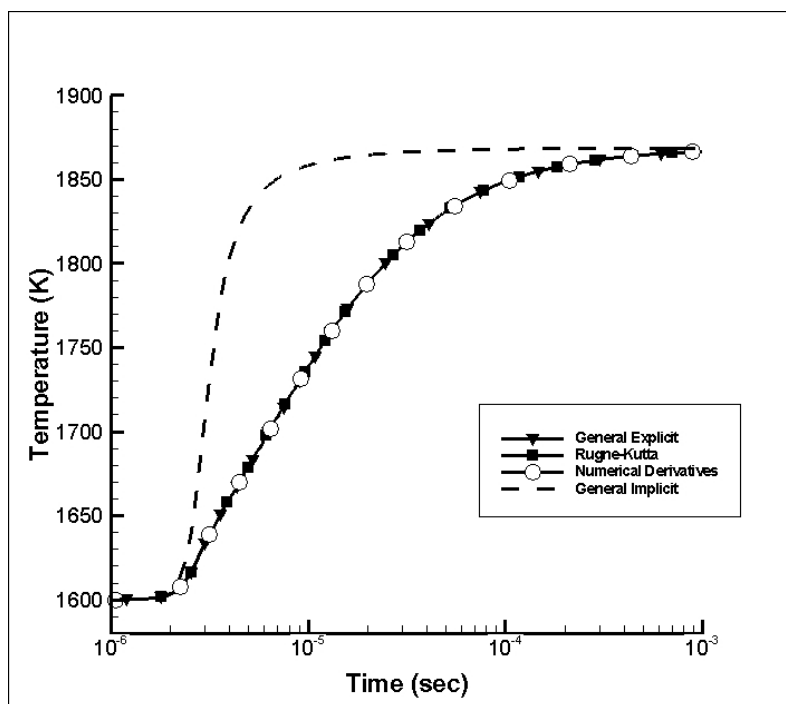


Figure 99. Temperature history for each numerical scheme using 7-step mechanism with a constant time step ($\Delta t = 1e-9$).

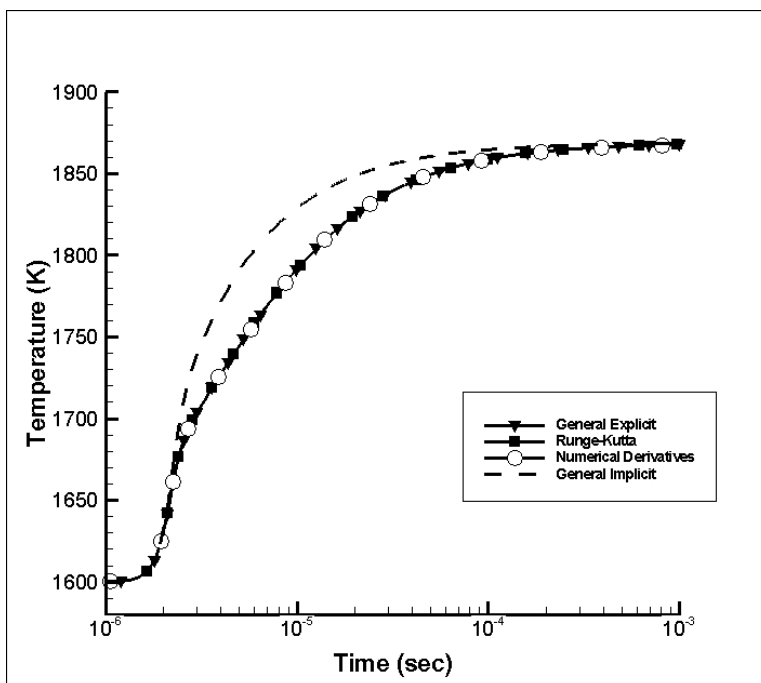


Figure 100. Temperature history for each numerical scheme using 19-step mechanism with a constant time step ($\Delta t = 1e-9$).

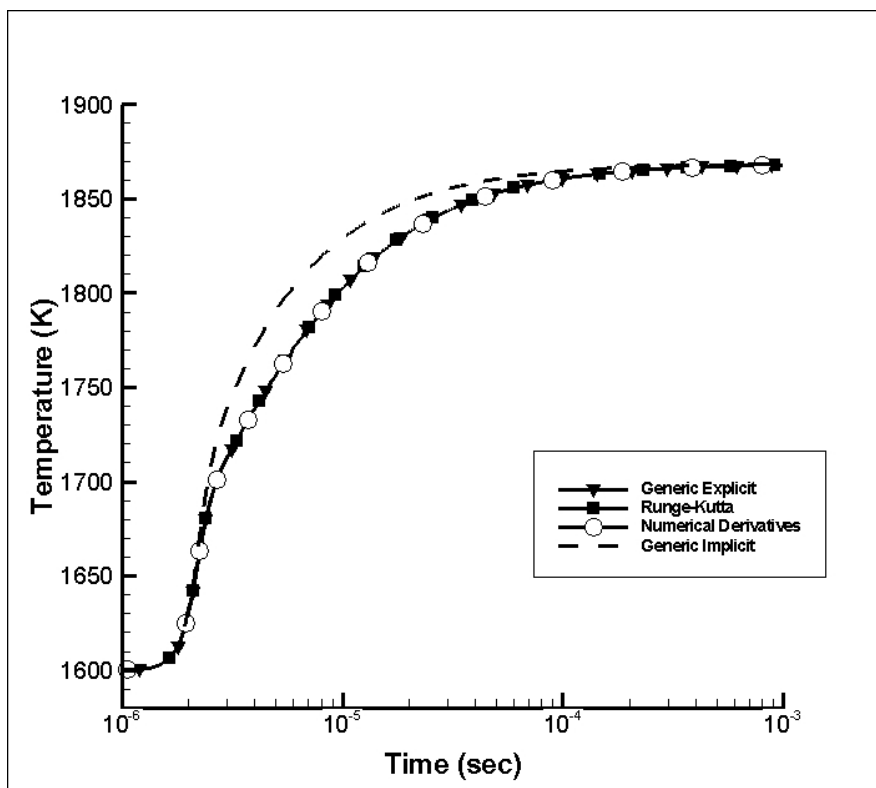


Figure 101. Temperature history for each numerical scheme using 32-step mechanism with a constant time step ($\Delta t = 1e-9$).

In this first set of results, the governing equations were integrated in time using a constant time step. This allows for the quantification of the computational requirements of each method. Table 4 shows the required run time for each method. All simulations were conducted on the same single processor, 3.0GHz desktop computer. The generic explicit method requiring the least run-time for each mechanism and the Runge-Kutta method also proved to be extremely efficient in the constant time step. This is due to the fact that no matrix operations are required. However, when using the explicit methods small time steps must be taken to maintain stability. Another possible occurrence is that the solution can produce non-physical solutions such as having mass fractions less than zero. Another notable result in Figure 102 is the times for the general implicit and numerical derivative methods. The generic implicit method required the greatest amount of run time to model the reactions due to the number of looping functions required to calculate the Jacobian terms. Results also show that the time saved by evaluating the Jacobian terms numerically grows as the mechanism becomes more complex. The increase between the two methods grew from 457% for the 7-Step mechanism to 1383% for the 32-Step mechanism. The numerical derivatives are, on average, approximately nine times more efficient than the generic implicit solution when run with constant time steps.

Scheme	Reaction Mechanism		
	7-step	19-step	32-step
General Explicit	335.00	546.00	821.00
Runge-Kutta	625.00	1555.00	3033.00
Numerical Derivatives	687.00	2118.00	5982.00
General Implicit	3845.00	19272.00	82715.00

Figure 102. Computational times in seconds using ($\Delta t = 1e-9$) for each reaction mechanism and solution scheme.

The true improvement and efficiency of the different schemes comes from the use of variable time steps. Unless the time step in the simulation is limited to resolve a process of interest, the desire is to integrate the governing equations through the time period as rapidly as possible. Therefore in the following simulations each scheme was allowed to set its Δt based on stability requirements and to keep the solution out of non-physical regions. A maximum allowable value for Δt was set to be 1E-5 seconds. Each reaction mechanism was again modeled with initial conditions of T=1600K and P=1125kPa and out to a time of one millisecond.

Figures 103, 104, and 105 show temperature histories for each scheme and mechanism using a variable time step. In order to retain accuracy the explicit methods had to be forced to take smaller time steps at the beginning of the calculations. The generic explicit results using a variable time step matches the results when the constant time step is employed. The numerical derivatives and generic implicit method have shapes similar to that of their constant time step solutions with the numerical derivative approach again more closely tracking the explicit results. This is due in part to the fact that the implicit method using the numerical derivatives was found to take smaller time steps initially. The generic implicit time history contains fewer points, thus it gives a rougher solution than the numerical derivatives method. This could easily be corrected by further restricting the time step of the generic implicit scheme to better capture the profile.

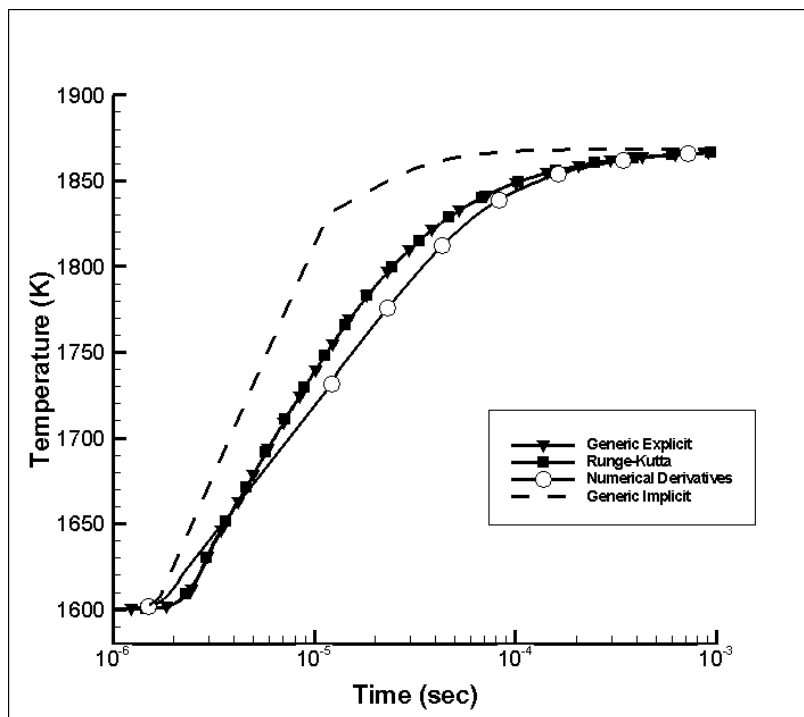


Figure 103. Temperature history for each numerical scheme using 7-step mechanism with a variable time step.

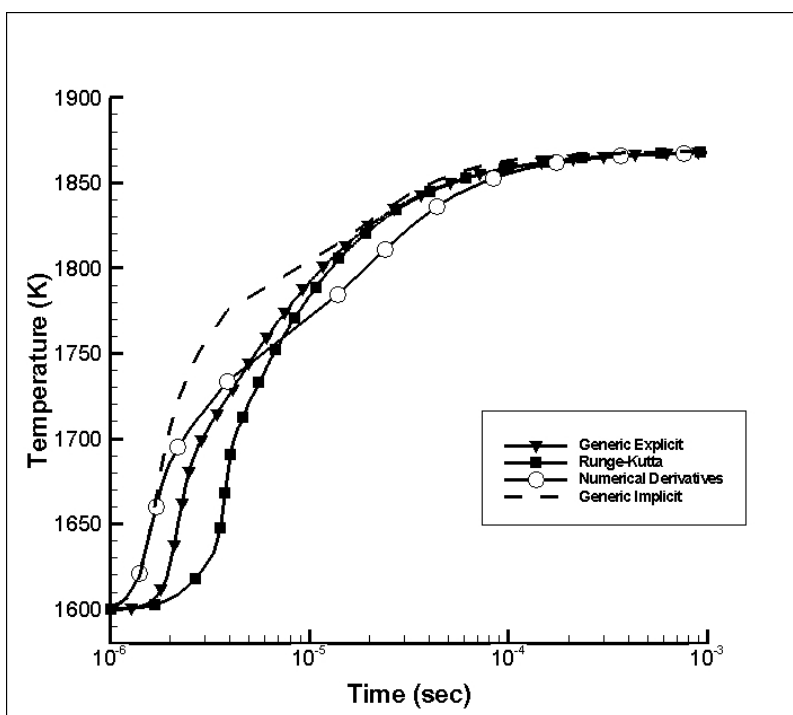


Figure 104. Temperature history for each numerical scheme using 19-step mechanism with a variable time step.

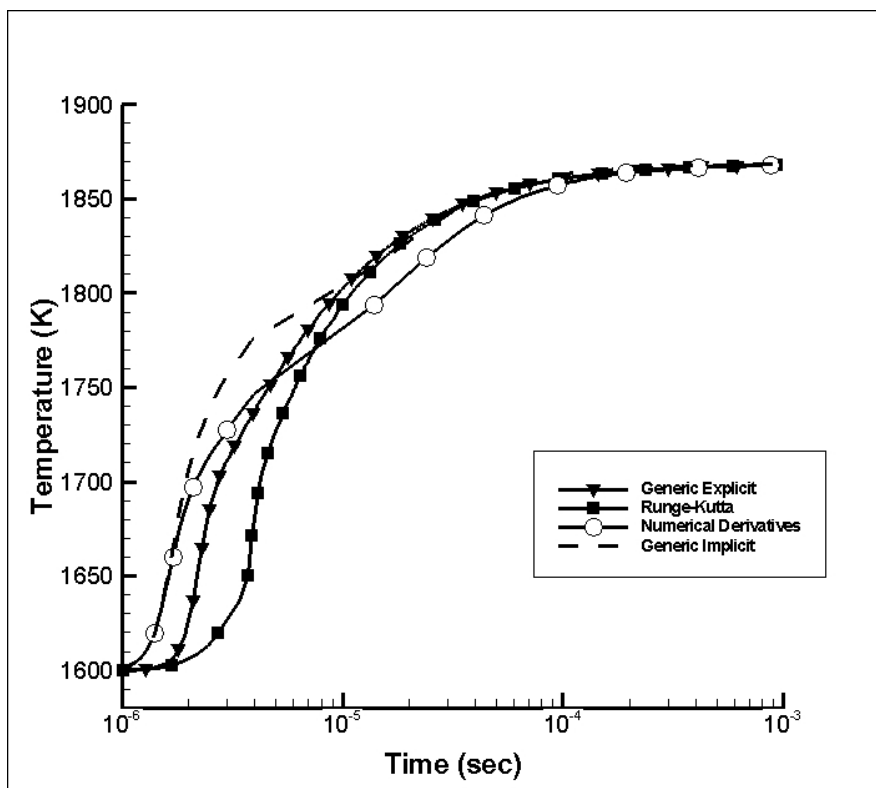


Figure 105. Temperature history for each numerical scheme using 32-step mechanism with a variable time step.

Scheme	Reaction Mechanism		
	7-step	19-step	32-step
General Explicit	77.00	163.00	571.00
Runge-Kutta	1464.00	2443.00	4987.00
Numerical Derivatives	3.000	4.000	5.000
General Implicit	4.000	6.000	12.000

Figure 106. Computational times in seconds using a variable time step for each reaction mechanism and solution scheme.

The run time results for each method when using a variable time step to solve the various mechanisms are shown in Figure 106. The overall run times are reduced due to the fact that the schemes are allowed to take the maximum time step they can and maintain a stable and physically possible solution. Employing the numerical derivatives is found to reduce the computational time and the advantage improves as the mechanism complexity increases. The advantage of using an implicit method is clear and can be attributed directly to the increased stability allowing for larger integration time steps. It should be noted that some

of the advantage will be diminished if the maximum allowable time step were reduced out of necessity to resolve important intermediate stages in the reaction process.

At the center of simulating reacting flow scenarios is the solution of the equations governing the combustion process. The two primary classes of methods are explicit and implicit. The explicit methods require much less computational resources per time integration step. However, due to stability requirements the time step when these methods are used have to be limited to small values. This is acceptable if a small step is desired to ensure resolution of intermediate chemical processes. However, it is more desirable to have an integration method that is not limited primarily by the numerical aspects.

Implicit methods offer advantages in terms on their stability and due to their nature the solutions tend to allow for larger time integration steps. Though the implicit schemes require considerably more computational time per step, these advantages overcome the shortfalls when considering the total time of the simulation. The typical implicit method uses several looping routines to construct the Jacobian matrix needed for the operations. By introducing numerical derivatives the resulting method is found to produce shorter run times and reduce the roundoff error. These initial results support further investigation into using numerical derivatives in the solution of the reaction equations found in combustion flow problems.

7. Results

Initially this project was utilizing a code titled *cutter* provided by the US Air Force Research Lab's Munition Directorate. We eventually had to shift to using an alternative computational framework to be able to pursue some of the topics of interest. Using the new framework to include the adaptive meshing the various detonation modeling strategies were evaluated. The case of an impact sending a shock into the explosive material was the scenario used and is depicted in Figure 107. This is patterned after the flyer plate problem that has been used to test the ignition-growth model in *cutter* [12]. Here a slug of air is used to impact the explosive since no constitutive models for inerts have been integrated into the current modeling framework.

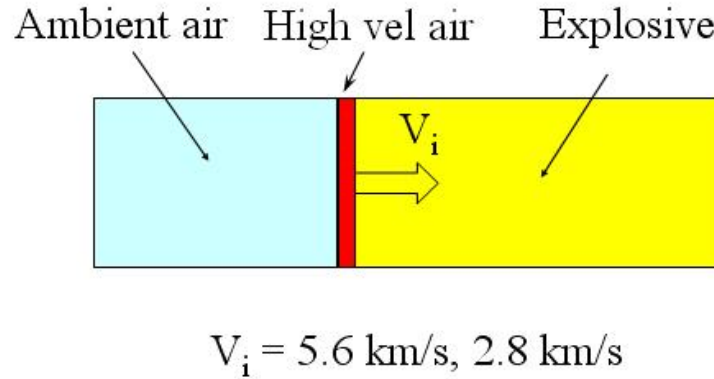


Figure 107. Configuration used in the shock initiation simulations.

To simulate these cases, the JWL equation of state was used for the unreacted explosive material and the detonation products with the parameters in Table 1. The first simulation cases used the ignition and growth model by [23] and demonstrated by [12]. The parameters for the reaction are listed in Table 2. Two impact cases were run with impact velocities of 2.8 km/s and 5.6 km/s. These two were selected because the lower velocity is known to not produce a self sustaining detonation but the higher velocity will [11].

	Unreacted Explosive	Detonation Products
ρ_o (g/cc)	1.624	-
A (GPa)	17101	673.1
B (GPa)	-3.745	21.988
R_1	9.8	5.4
R_2	.98	1.8
ω	.5675	.3
C_v (GPa/K)	2.70386e-3	1.0e-3
E_o (GPa)	0	7.0

Table 1. JWL EOS Parameters for the TNT and detonation products.

Reaction Rate Parameters
$l=5.0e7$
$a=0$
$b=.667$
$x=4.0$
$G_1=3.6e8$
$y=1.2$
$c=1.0$
$d=.667$
$G_2=0$
$e=1.0$
$g=.111$
$z=1.0$
$F_{igmax}=0.03$
$F_{G1max}=1.0$
$F_{G2min}=0.0$

Table 2. JWL EOS Parameters for the TNT and detonation products.

7.1 Single Step Models

The first reaction models tested were those that use a single step to represent the reactions involved in the detonation. Figures 108, 109, and 110 are a sequence of images showing the predicted response of the TNT using the ignition and growth when impacted at 2.8 km/s. A compression wave is seen to travel through the energetic material and associated heating occurs. However, a self-sustaining detonation is not produced. For this simulation only one level of cells was used. Figures 111, 112, and 113 show the response when the impact velocity is raised to 5.6 km/s. In the pressure data, the von Neumann pressure behind the shock of the detonation front is evident and the value is consistent with the experimental data. The detonation forms and is self sustained through the full length of the explosive.

Figures 114, 115, and 116 show the 5.6 km/s case results when two levels of computational cells are used. The parameter e plotted with the velocity is the adaptation parameter (ε) discussed earlier. Using two levels does not offer much advantage for the 1D impact problem but was tested here.

The results using the ignition and growth model demonstrate correct response to impact and produce the correct data in terms of post detonation pressure. However, the temperatures determined using the JWL EOS data are not correct. The detonation temperature for TNT is known to be approximately 3700 K. This is not a surprise since the JWL EOS was not formulated with the

intention to correctly predict temperature. The ignition and growth model does not even use this variable in its calculation. However, this is a shortcoming if a single reaction model is desired to predict all possible reaction scenarios.

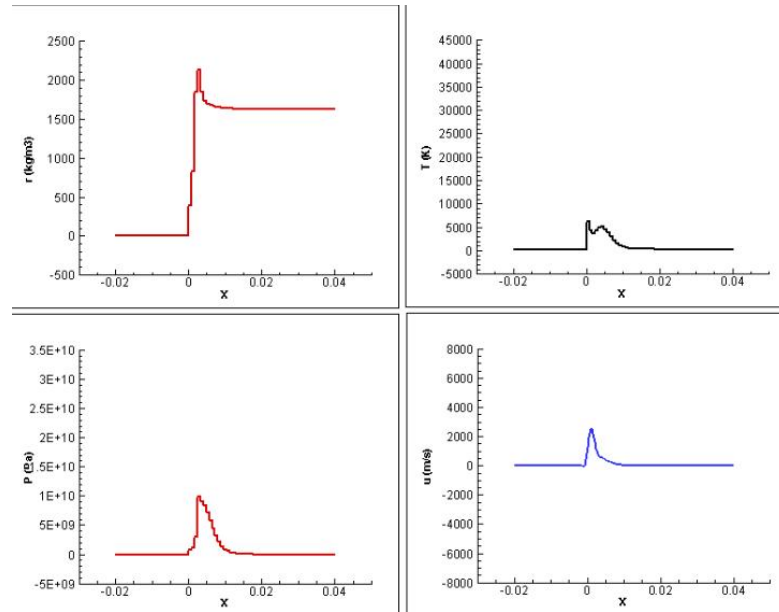


Figure 108. Sequence of images showing the results using the ignition and growth model and a single level of cells for the $V_i = 2.8 \text{ km/s}$ case shortly after impact.

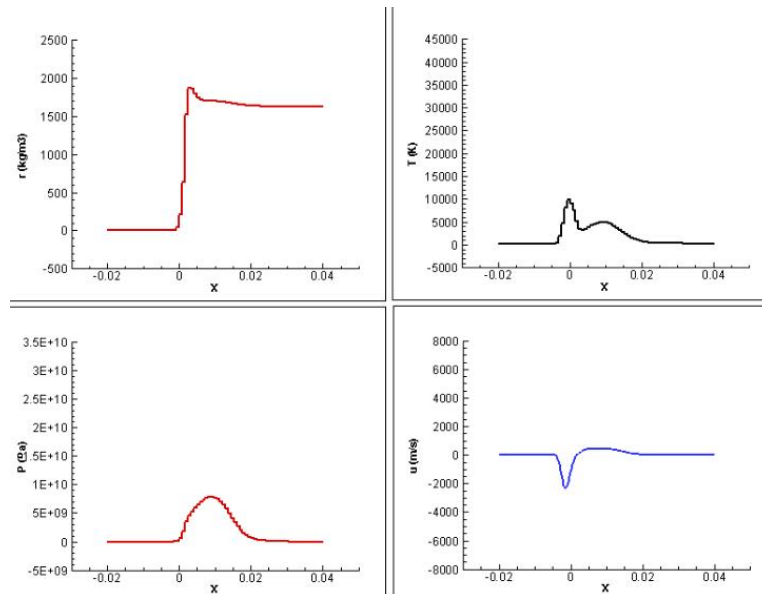


Figure 109. Image showing the results using the ignition and growth model and a single level of cells for the $V_i = 2.8 \text{ km/s}$ case some time after impact. No self sustaining detonation has formed.

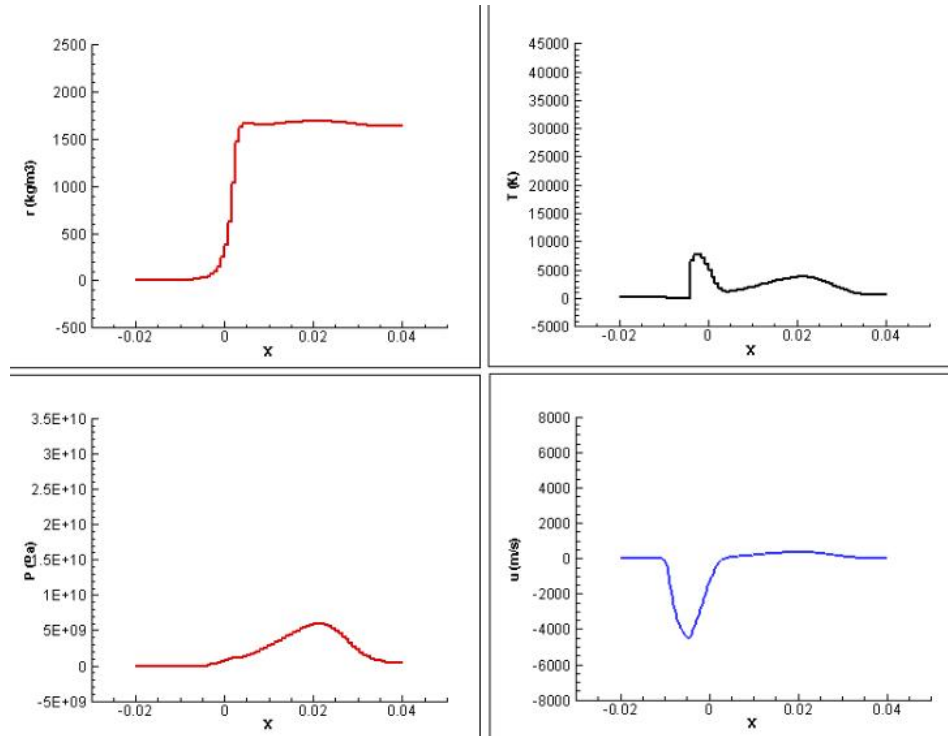


Figure 110. Image showing the results using the ignition and growth model and a single level of cells for the $V_i = 2.8 \text{ km/s}$ case well after impact. No self sustaining detonation has formed.

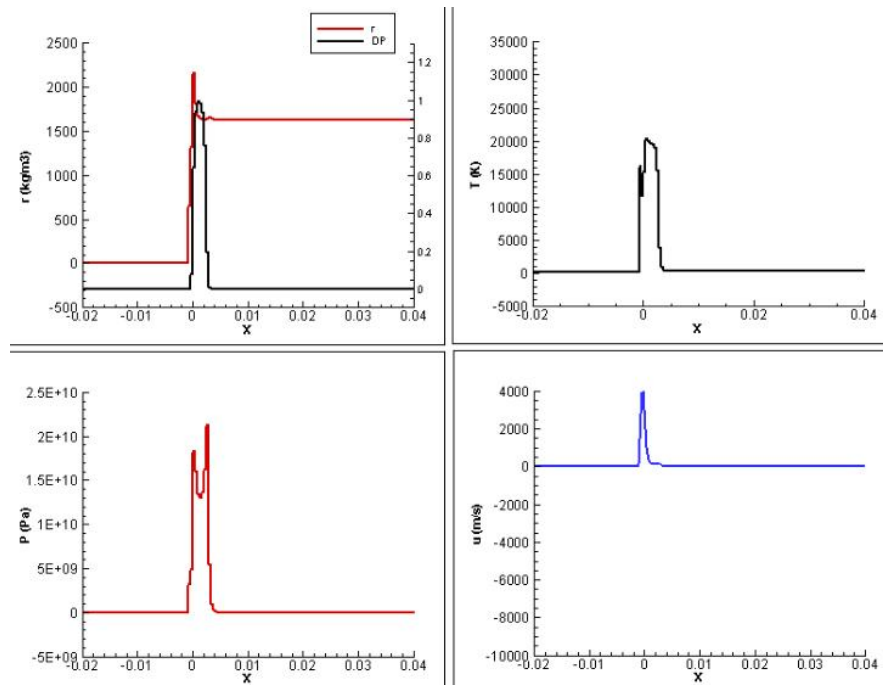


Figure 111. Sequence of images showing the results using the ignition and growth model and a single level of cells for the $V_i = 5.6 \text{ km/s}$ case shortly after impact.

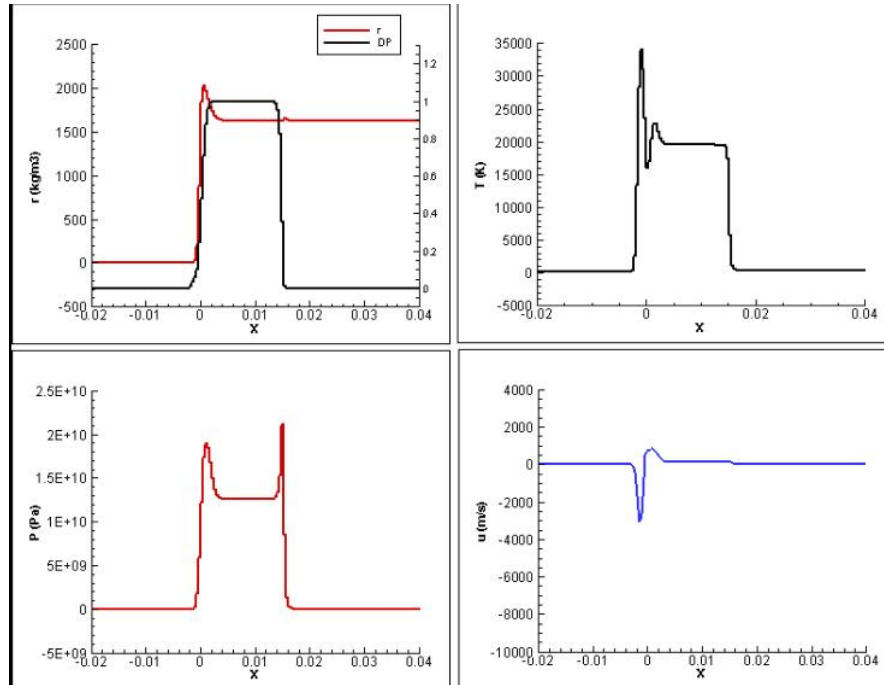


Figure 112. Image showing the results using the ignition and growth model and a single level of cells for the $V_i = 5.6 \text{ km/s}$ case some time after impact. A self sustaining detonation has formed.

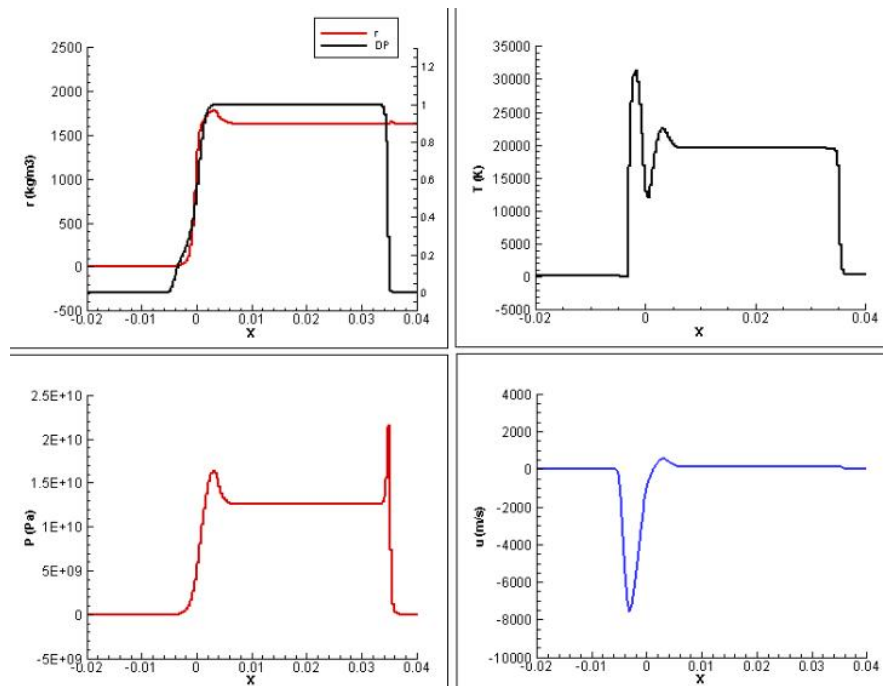


Figure 113. Image showing the results using the ignition and growth model and a single level of cells for the $V_i = 5.6 \text{ km/s}$ case well after impact and the formation of the self sustaining detonation.

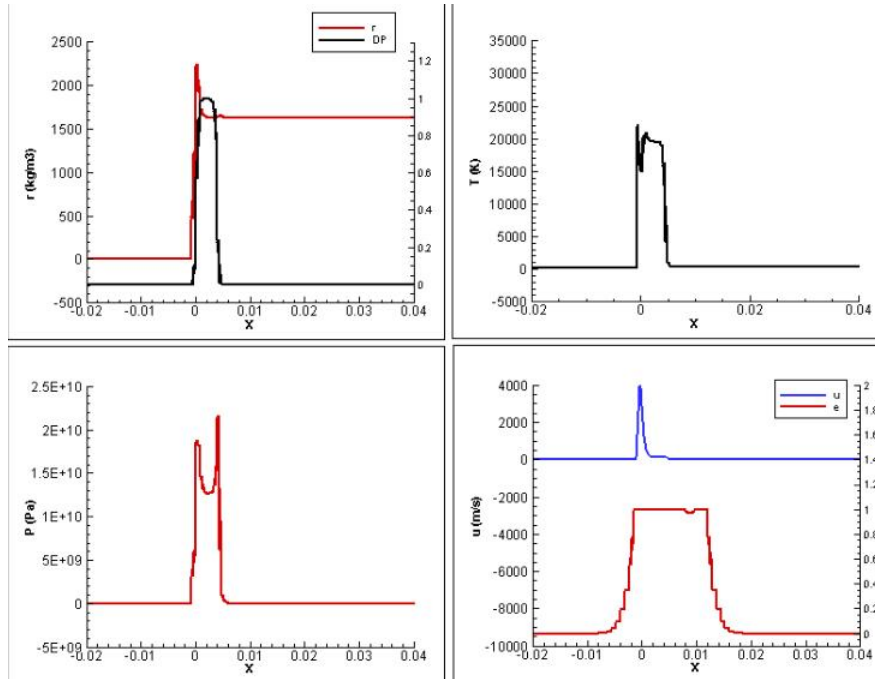


Figure 114. Sequence of images showing the results using the ignition and growth model and two levels of cells for the $V_i = 5.6 \text{ km/s}$ case shortly after impact.

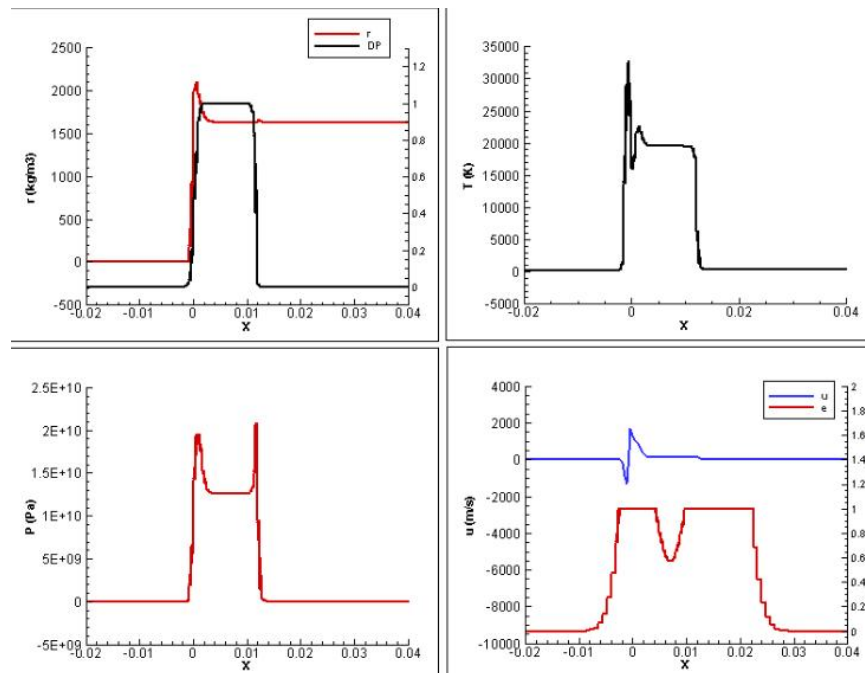


Figure 115. Image showing the results using the ignition and growth model and two levels of cells for the $V_i = 5.6 \text{ km/s}$ case some time after impact. A self sustaining detonation has formed.

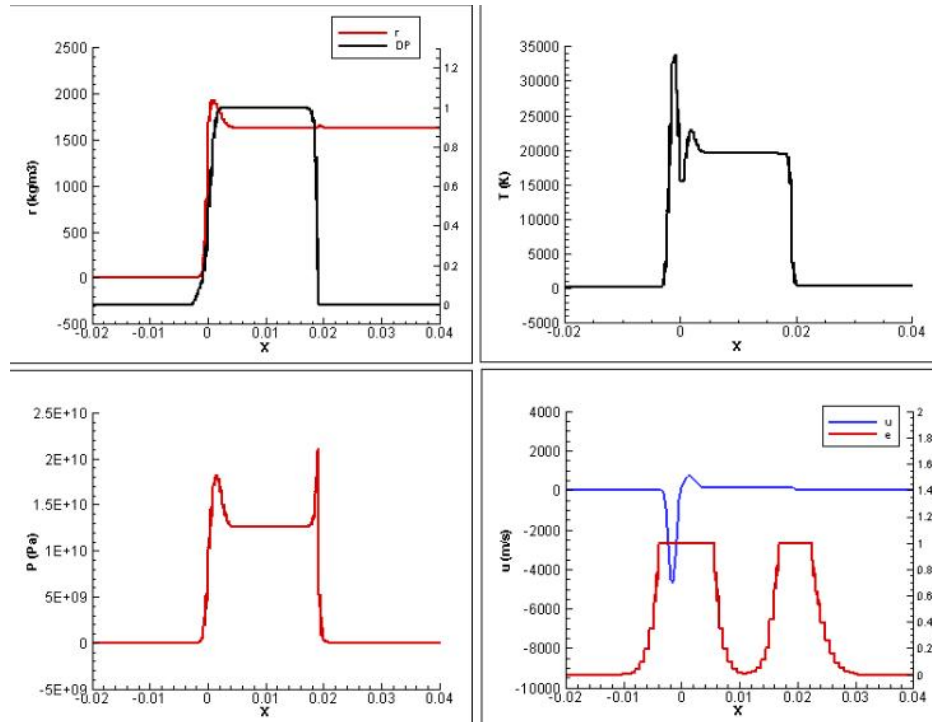


Figure 116. Image showing the results using the ignition and growth model and two levels of cells for the $V_i = 5.6 \text{ km/s}$ case well after impact and the formation of the self sustaining detonation.

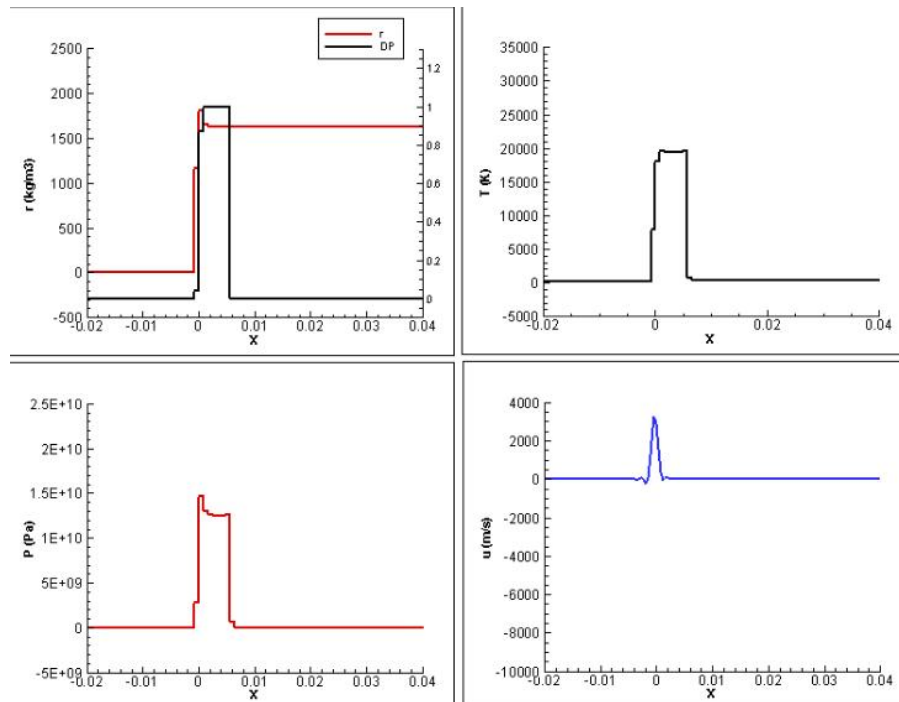


Figure 117. Images showing the results using the hot spot and balance model and a single level of cells for the $V_i = 2.8 \text{ km/s}$ case shortly after impact.

Figures 117 and 118 are a sequence of images showing the predicted response of the TNT using the hot spot and balance model when impacted at 2.8 km/s. Figures 119, 120, and 121 show the results for the 5.6 km/s case. The results are seen to be similar to those from the ignition and growth model. Again the pressure and wave dynamics are correctly captured but the temperature profiles are not accurate. The hot spot and balance model is a temperature based reaction model however since the material model does not accurately predict temperature in the shocked material, the model is not that sensitive to the actual temperature. This insensitivity is clear if the formation of the model is reviewed. The temperature dependence is derived by using the known detonation pressure and induction time for the material. In the work by [17] the Mie-Gruneisen equation of state was used so the calculated temperature is different and is reported to be more consistent with the known detonation temperature.

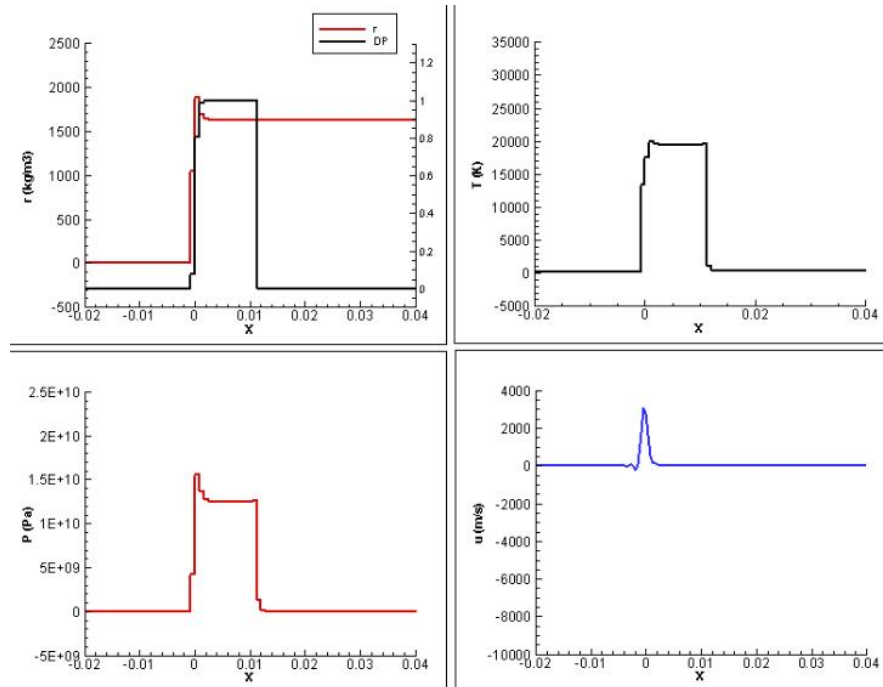


Figure 118. Images showing the results using the hot spot and balance model and a single level of cells for the $V_i = 2.8 \text{ km/s}$ case some time after impact.

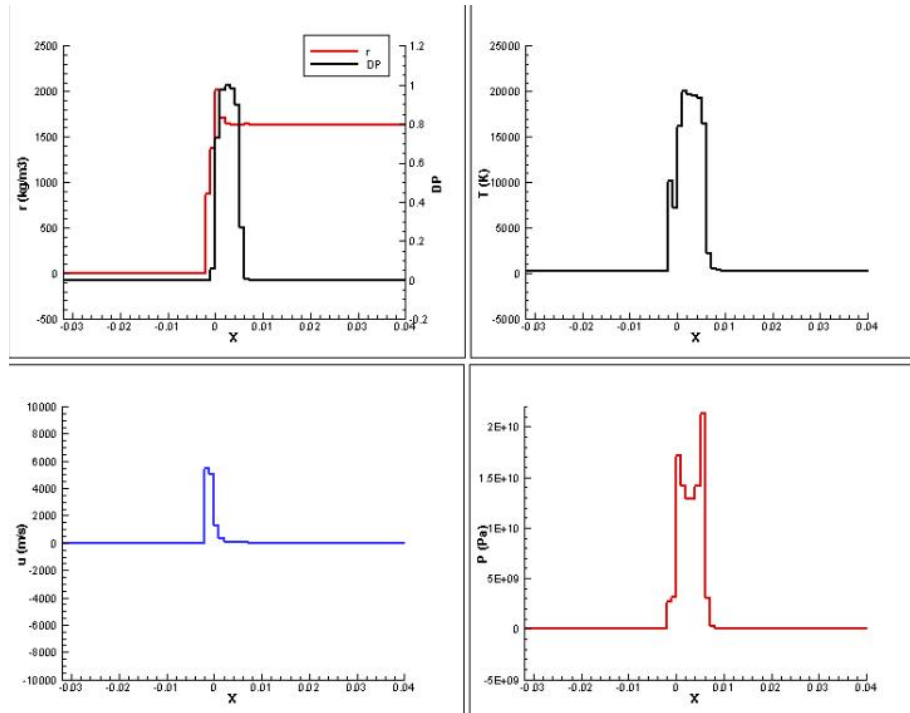


Figure 119. Images showing the results using the hot spot and balance model and a single level of cells for the $V_i = 5.6 \text{ km/s}$ case shortly after impact.

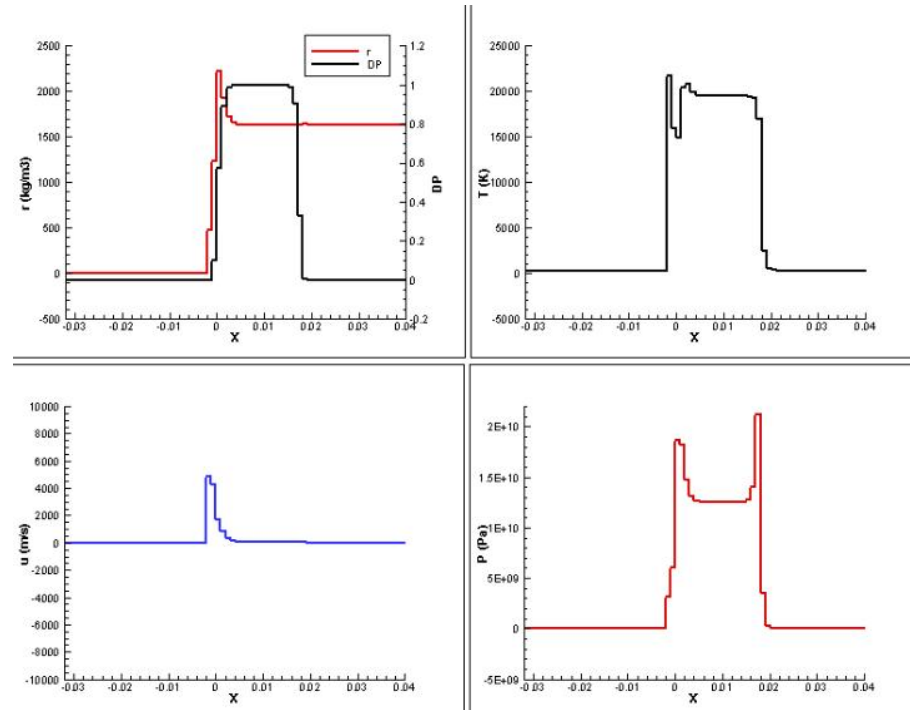


Figure 120. Images showing the results using the hot spot and balance model and a single level of cells for the $V_i = 5.6 \text{ km/s}$ case some time after impact. A self sustaining detonation has formed.

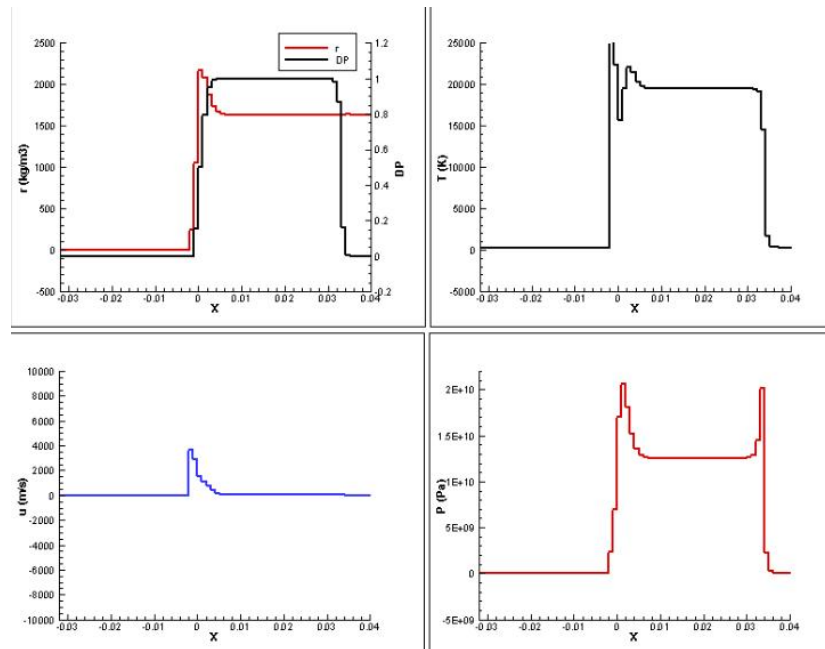
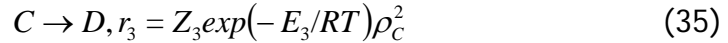
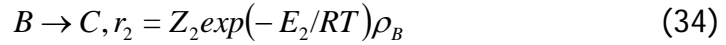
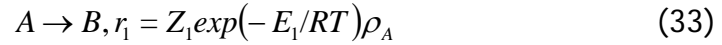


Figure 121. Images showing the results using the hot spot and balance model and a single level of cells for the $V_i = 5.6 \text{ km/s}$ case well after impact and the formation of the self sustaining detonation.

7.2 Multi-step, Finite-rate Model

The single-step kinetics models perform adequately when the interest is to reproduce the travel of the detonation wave. However, they do not offer a wide range of applicability and will not accurately model all scenarios of interest. As mentioned, one objective of this project was to determine the feasibility of having a kinetics based model that could correctly represent a wide range of scenarios involving energetic materials. The range of possible scenarios run from slow events such as cook-off to the case of detonations. The recent, successful work in using multi-step, finite-rate models in simulating cook-off [40] provided a good point of departure.

In this earlier study, the decomposition of the explosive RDX was represented using a three-step, four-species model of the form



where A and B are solid species, and C and D are gases. The parameter r_i is the reaction rate and Z_i is the rate factor and E_i is the activation energy for reaction i . This form is similar to the Arrhenius rate law typically used in gas phase combustion modeling. The parameter ρ_j is the mass fraction of species j . The parameters for the RDX decomposition can be found in Table 3. Here this baseline model will be used for the detonation case to see how it performs. Prior to that, the one-dimensional-time-to-explosion (ODTX) case for the RDX simulated by [40] was recreated.

Reaction step	$\ln Z_k$	E_k (kJ/g mole K)	q_k (J/g)
$A \rightarrow B$	$43.70s^{-1}$	197.2	139.0
$B \rightarrow C$	$38.90s^{-1}$	184.7	-535.6
$C \rightarrow D$	$32.69cm^3/sg$	142.8	-4680

Table 3. Reaction kinetics parameters for the decomposition of RDX.

The ODTX scenario is modeled using the chemical reaction source model discussed earlier and the time to explosion was determined for a range of

temperatures. In the simulations the fluid dynamics operations can be ignored and a mass of explosive is suddenly increased to the specified temperature. The time history of the species concentrations and the temperatures were recorded and presented in Figure 122. Figure 123 summarizes the predicted times to explosion as a function of temperature. Also shown in the figure are the results from the earlier study [40] and experimental data. The current results show shorter times to explosion for the higher temperatures than those predicted in the earlier study and the few experimental points in that region. However, at the lower temperatures the current results compare well with the experimental data.

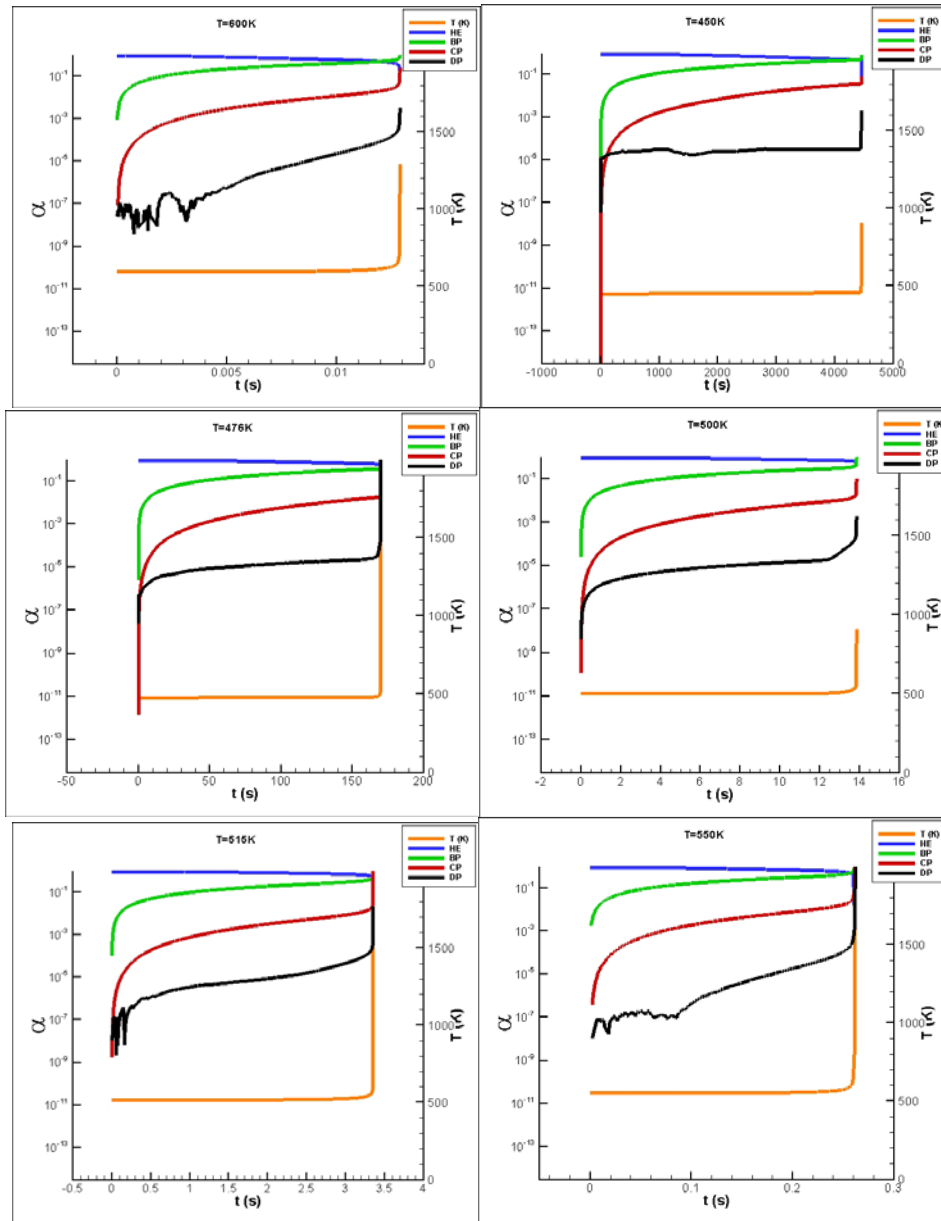


Figure 122. Time histories recorded at different initial temperatures in the one-dimensional-time-to-explosion (ODTX) simulations.

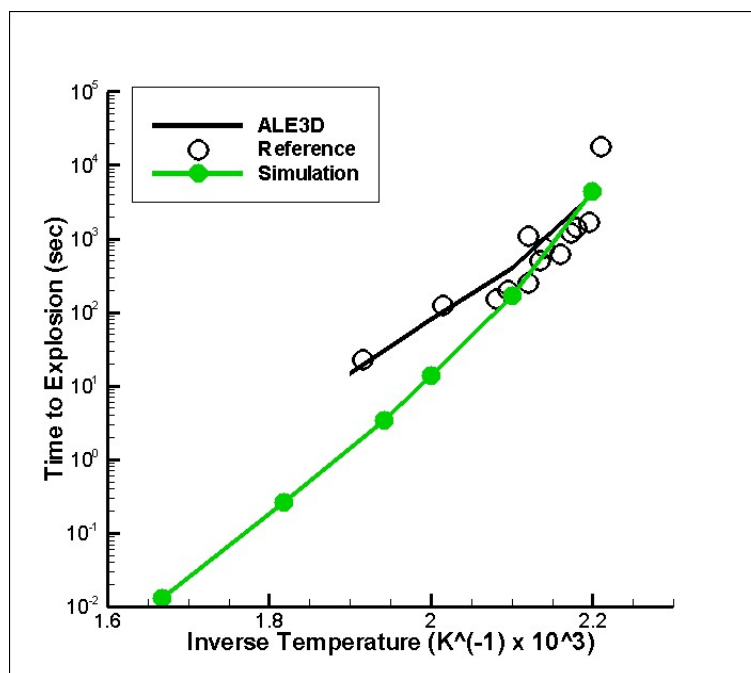


Figure 123. Calculated ODTX times using the current model compared to experimental data and earlier studies.

This three-step, four-species model was tested within the context of the impact scenario run with the one-step models. The 5.6 km/s case was run and sample results are shown in Figures 124, 125, and 126. The solution shows that a shock is driven through the energetic material by the reaction front, however the pressure does not reach the von Neuman value and the front speed is not equal to the known detonation velocity. This is not a surprise since the reaction paths and time scales for the detonation regime will be different for the cook-off regime for which the current model was developed. In the next section some initial work will be presented related to modifying the mechanism to also cover the detonation regime.

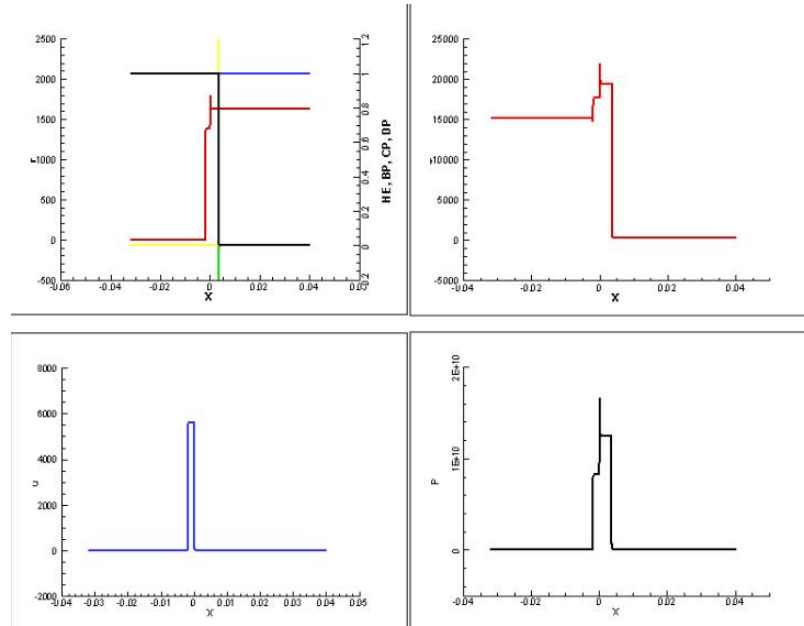


Figure 124. Images showing the results using the multi-step, finite-rate model and a single level of cells for the $V_i = 5.6 \text{ km/s}$ case just after impact.

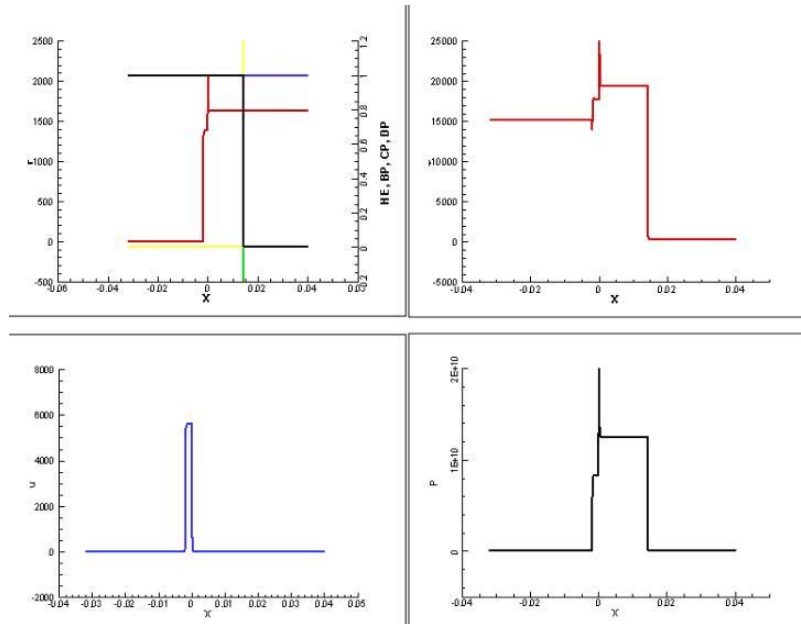


Figure 125. Images showing the results using the multi-step, finite-rate model and a single level of cells for the $V_i = 5.6 \text{ km/s}$ case shortly after impact.

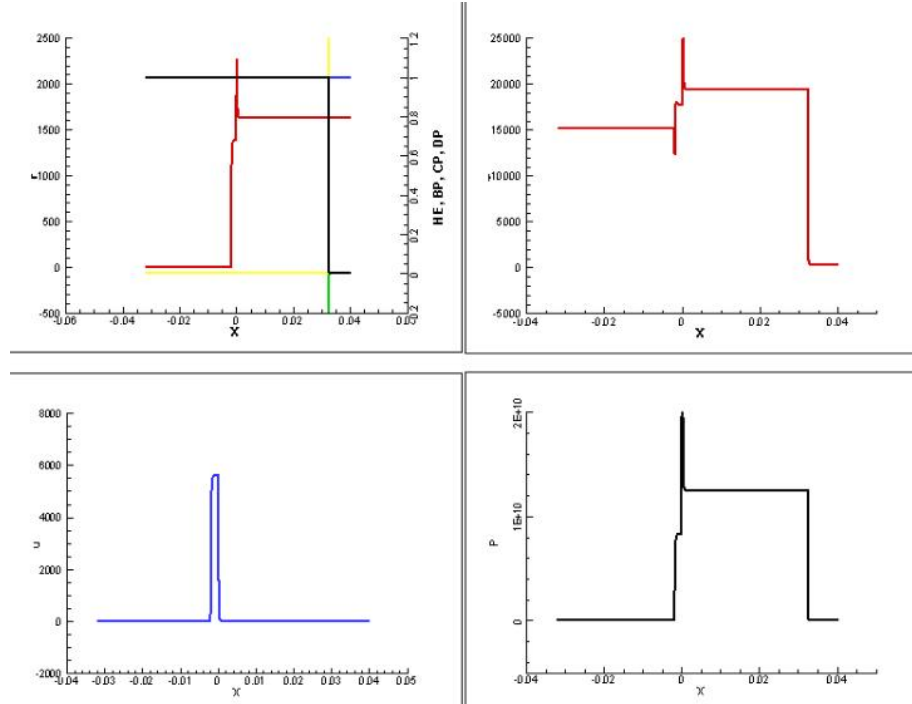


Figure 126. Images showing the results using the multi-step, finite-rate model and a single level of cells for the $V_i = 5.6 \text{ km/s}$ case some time after impact.

In the earlier work by [40], a one-step model was used to simulate the travel of the detonation after initiation from the thermal explosion process. The model was used here to simulate the impact scenario for which the other one-step models were used. Since this model is designed for the detonation regime just the 5.6 km/s case was simulated and the results are shown in Figures 127 and 128. The model is seen to produce the correct von Neumann pressure. Figure 130 compares the predicted time histories of pressure at a location in the explosive for the detonation case for each one-step model and the three-step model. The one-step models provide similar predictions of the pressure profiles but the arrival times vary.

The three-step model is found to not produce the von Neumann spike known to exist. This may be due to the fact that since the reaction process in the detonation is being represented by a multi-step model, the required resolution is extremely rigid. This can be overcome using the adaptation methods detailed here. However, it would be desirable to have a model that might require grid adaptation for exact resolution but not be totally dependent on the grid to show the general nature of the phenomena. It is clear that all 1-step models do reproduce the general trend. A strategy to combine the characteristics of the multi and single step models will be presented in the next section.

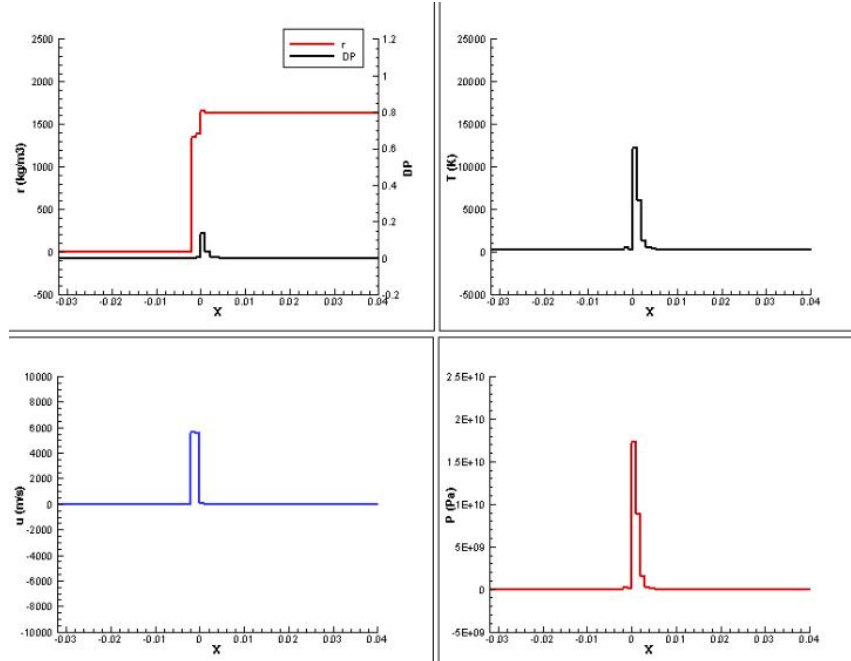


Figure 127. Images showing the results using the hot spot and balance model and a single level of cells for the $V_i = 5.6 \text{ km/s}$ case shortly after impact.

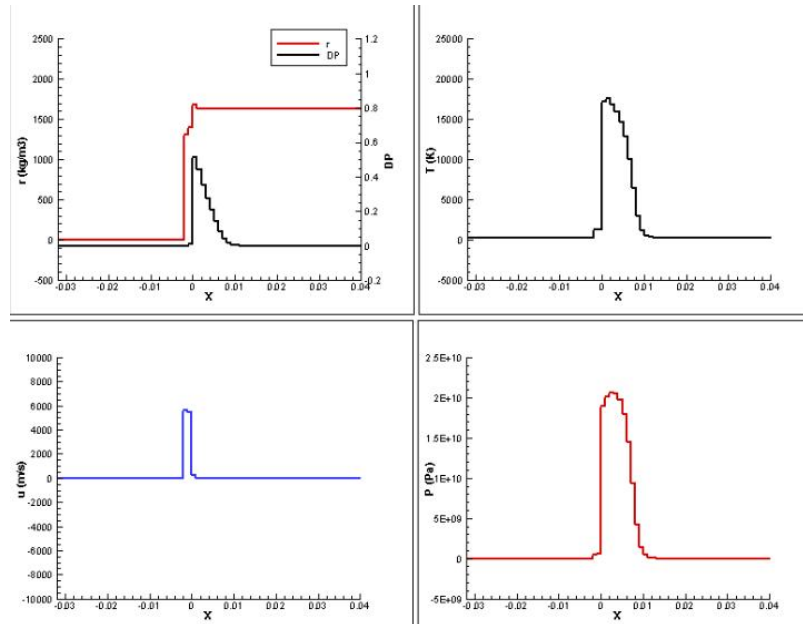


Figure 128. Images showing the results using the hot spot and balance model and a single level of cells for the $V_i = 5.6 \text{ km/s}$ case some time after impact. A self sustaining detonation has formed.

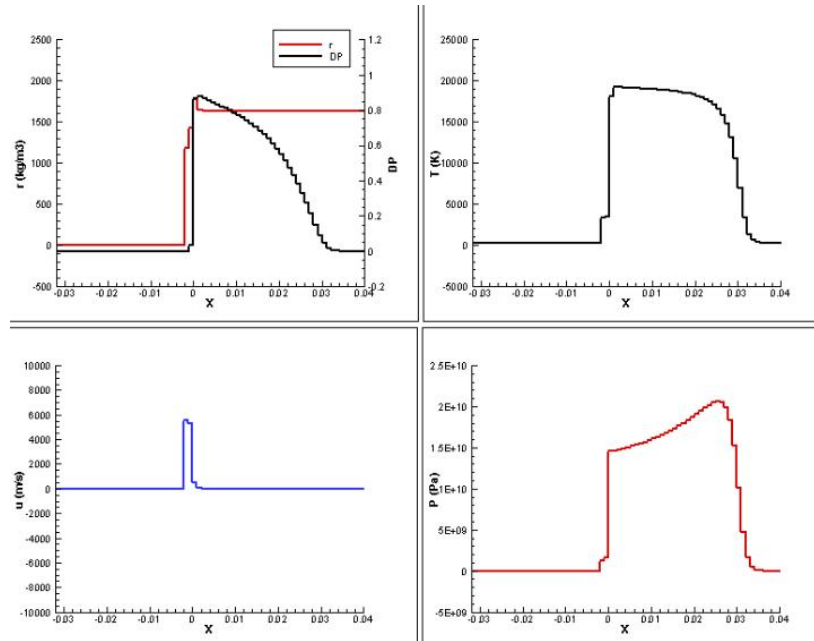


Figure 129. Images showing the results using the hot spot and balance model and a single level of cells for the $V_i = 5.6 \text{ km/s}$ case well after impact and the formation of the self sustaining detonation.

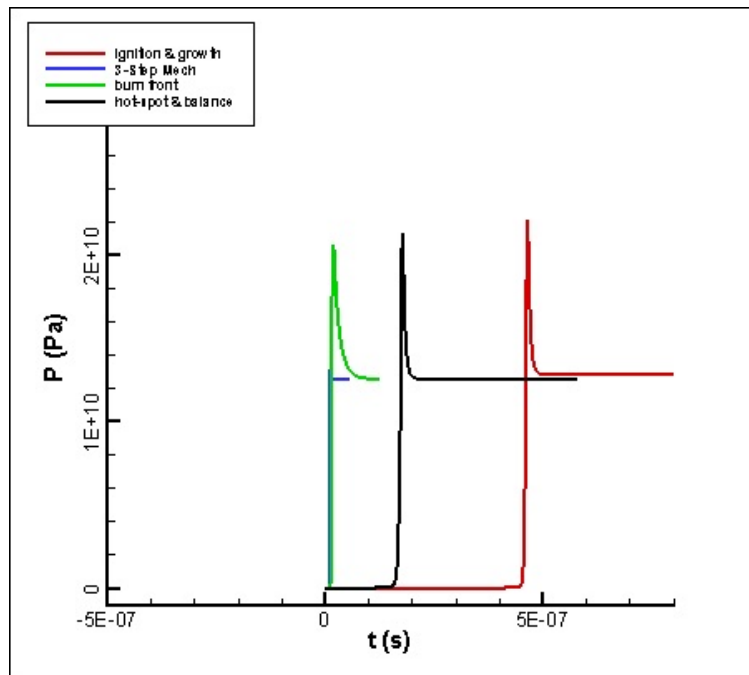


Figure 130. Comparison of the predicted pressure profiles for the detonation case using the various one-step models.

7.3 Modified Multi-step, Finite-rate Model

As shown here, a single-step reaction model is sufficient to represent a detonation process. Though the rate based models are dependent on local conditions a multi-step model is needed to represent the full spectrum of reaction scenarios, an objective of this project. As shown, the multi-step models like that used by [40] can represent these other processes. However, it is found to not easily show the detonation case and when used in the earlier study a *switch* is made from the multi-step model to a simpler 1-step model once an *explosion* occurs. This switching process would be difficult to make autonomous and an elaborate method would be needed if the detonation mode needed to be *switched* back to the deflagration case. A universally application approach may be possible by incorporating characteristics used in other combustion problems.

Multi-step, finite-rate reaction models are routinely used to model a wide range of combustion processes. With enough steps, multiple reaction paths are adequately represented. By representing the multiple reaction paths, a full range of combustion scenarios can be simulated. One example is how mechanisms can represent the explosion limits of fuel-oxidizer mixtures. An example can be seen in the hydrogen-air mechanisms in Figures 96 and 98. Though there is a difference of 25 steps, both reproduce slow burning and explosion scenarios. This can be shown by looking at results from an earlier study ([10]) using the two mechanisms in simulating shock initiated combustion, similar to a detonation.

Figure 131 shows an experimental image of the scenario which is a projectile shot into a mixture of hydrogen and air. The curved shock is visible. Also shown is the computed results of induction time of the mixture depending on which part of the shock the mixture crosses. The conditions on the respective streamline behind the shock (point 2 in the insert in Figure 131) are used to integrate the reaction equations. At locations of the curved shock when the shock angle is greater than approximately 50° , relative to the streamline, the induction time is long. Otherwise they are very short.

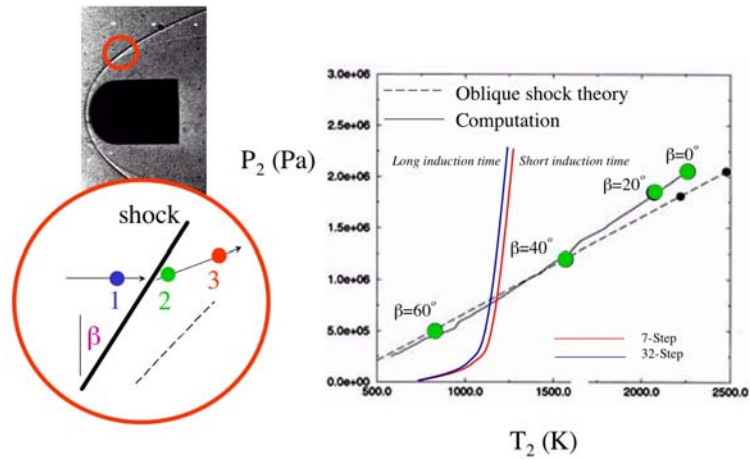


Figure 131. Shock initiated combustion scenarios and predicted induction times.

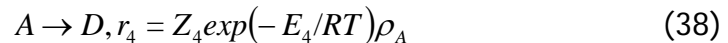
In the hydrogen-oxygen example, the explosion limit is controlled by the branching reaction



and the terminating reaction



where M represents any compound in the mixture. These *third body reactions* are highly dependent on pressure. Therefore, the local conditions to include pressure dictate whether a slow combustion process occurs or a detonation is produced by the model. A similar approach is possible for use for the current energetics problems. To test this idea, the multi-step model represented by Equation (33), (34), and (35) is augmented with the additional step



which represents an alternative reaction path. Figure 132 shows the relative rates at which each reaction occurs as temperature increases. The rate of the step represented in Equation (38) was set such that it would be dominate at the higher temperatures. The reaction step could also be fashioned to be dependent of pressure.

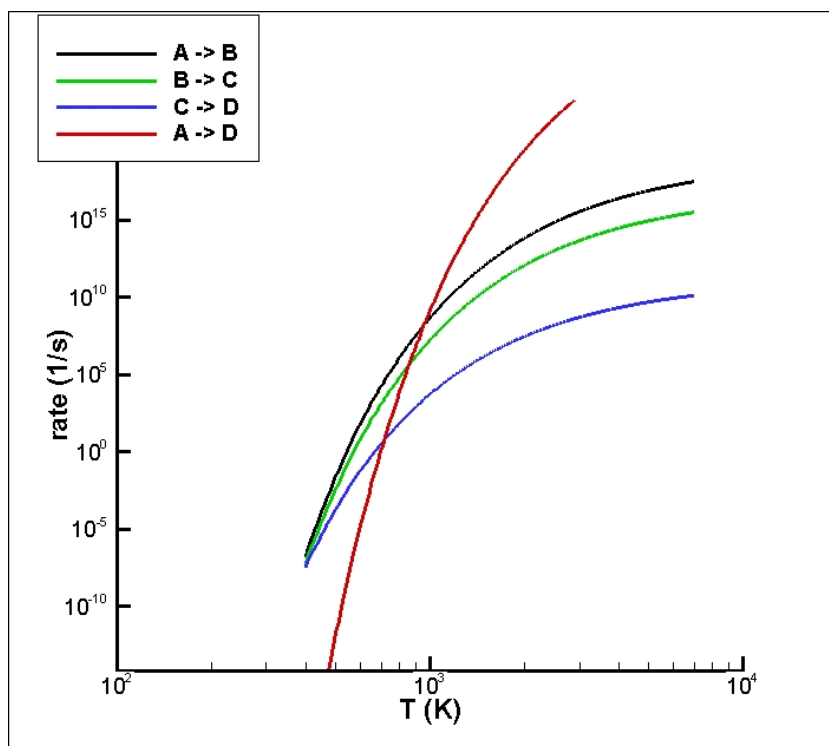


Figure 132. Comparison of the rates for each step in the modified model.

This 4-step model is compared to the original 3-step model by seeing how it responds to the same initial conditions. This is done by comparing the predicted time histories. One way is to plot the mass fraction of each material as a function of time as shown in Figure 133. Another useful comparison can be made by plotting various material concentrations versus others. In Figure 133 the intermediate products B and C are plotted as a function of the final product D. The 3-step and 4-step results, which are identical, of course start with $D=0$ and terminate when $D=1$. The symbols denote intervals in the integration and are evenly spaced in time. The reaction is seen to process slowly with B and C increasing up to a point and it then rapidly converges to the final state.

Similar results are seen when the the initial temperature is set to 600K as shown in Figure 134. However, the slope early in the process and the location of the transition changes. But when the initial temperature is set to 1000K, there is a distinct difference in the 3-step and 4-step results. As evident in Figure 135, the 3-step model shows results similar to the lower temperatures but the transition occurs much earlier. The highly nonlinear nature of the reaction process is one reason the integration of the multi-step models are much more difficult. When the 4th step is added to the model, this higher initial temperature causes the reaction to immediately move through the transition state to the final state. This is due solely to the alternate reaction path introduced to the model. Figure 136 shows a variety of comparisons by plotting various material

concentrations versus others. Introducing these alternative reaction paths appear to be a valid strategy for having a single reaction model that covers all possible reaction scenarios.

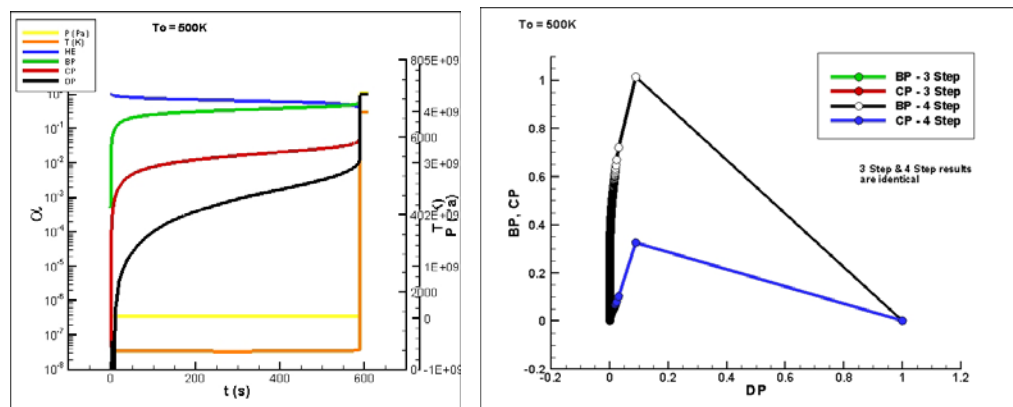


Figure 133. Comparison of the 3-step and 4-step reaction model results with an initial temperature of 500K.

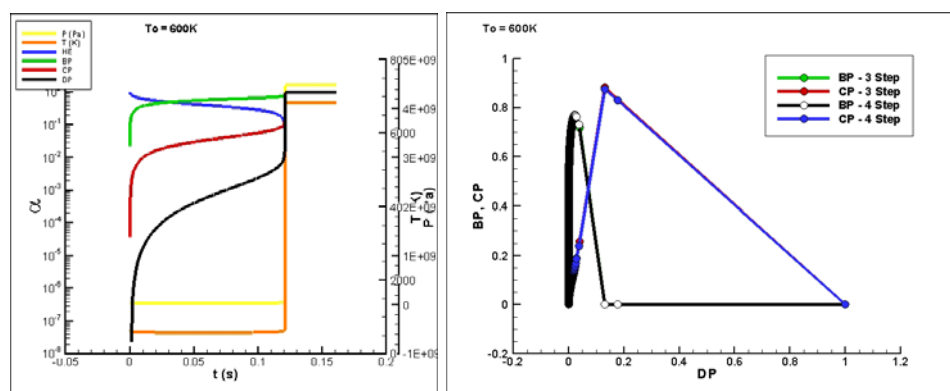


Figure 134. Comparison of the 3-step and 4-step reaction model results with an initial temperature of 600K.

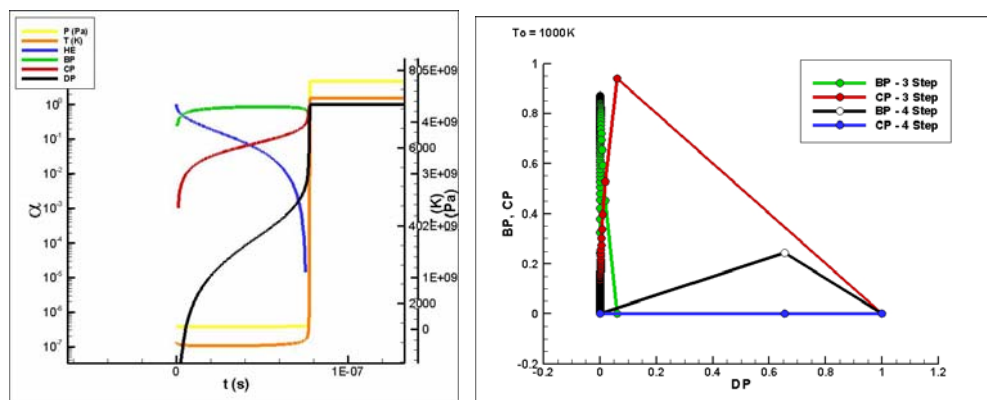


Figure 135. Comparison of the 3-step and 4-step reaction model results with an initial temperature of 1000K. The plot showing concentration as a function of time is from the baseline 3-step model since the 4-step transitions immediately to the final state.

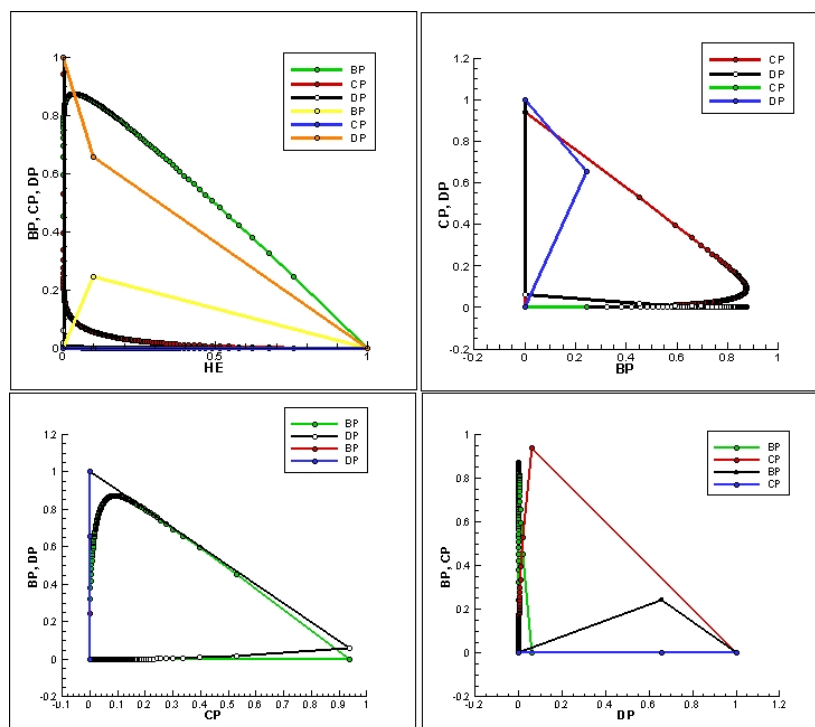


Figure 136. A variety of species space plots from the 3-step and 4-step reaction model results with an initial temperature of 1000K.

7.4 Example Full Weapon System Simulation

The ultimate objective is to have a modeling strategy that correctly simulates a variety of munition problems. One example is the case of premature burning of energetic materials in a weapon system due to mechanical stresses during employment. Such a situation could cause the weapon to not provide the full impact desired when initiation occurs since some of the energy would have already been released at a rate slower than the detonation case. The methods proposed here can be coupled together to provide such a modeling tool.

To demonstrate the use of the multi-step reaction model with the adaptive meshing framework, a weapon system scenario was simulated. The system is a typical penetrating warhead filled with explosive material. To demonstrate the strategy a portion of the explosive bed was heated at a temperature that would be produced during a mechanical stressing process. Figure 137 shows a sequence of images showing the temperature and pressure profile along a plane through the center of the item. The general process is captured and the progression of the burning is tracked. The simulation was not run to the point of detonation. To fully simulate this scenario an additional thermal model to include heat transfer through the energetic bed would be needed.

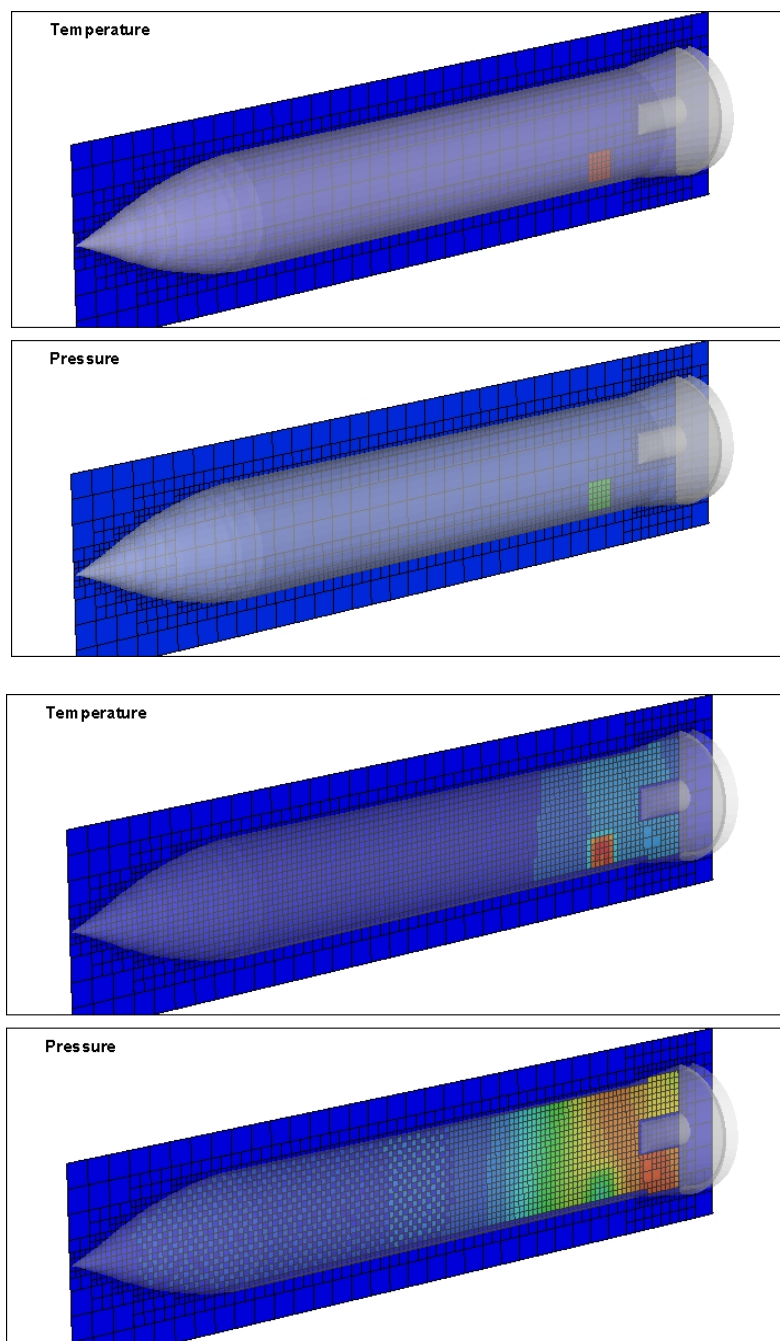


Figure 137. Sequence of images showing the solution of the three-step reaction model for a full system simulation.

8. Findings and Future Work

Kinetics based modeling of detonations is a viable and reliable simulation option. Here a variety of 1-step model types have been investigated and all

provide the same general results. However, these single reaction path models do not offer an option to simulate off detonation cases. To correctly simulate these scenarios a multi-step model is needed.

A multi-step model previously used to simulate cook-off type scenarios was tested for the detonation case. It was found to not provide accurate results. This was due in part to the fact that the mechanism was not designed to cover this regime. However it was shown that by augmenting the basic mechanism with an additional reaction path the response to the detonation case is more in line with the 1-step models. This allows for the reaction model to dynamically *switch* depending on the local conditions. It also relaxes some of the numerical stiffness of the equation system.

Multi-step reaction models have been used for quite some time in the simulation of gas phase combustion. The same general approaches can be applied to the reaction of solid phase energetics. Some of the delay in using these approaches for this class of problems has been the numerical aspects of the problem. Advancing techniques such as the numerical derivative approach shown here should provide robust modeling tools. This approach also allows for any reaction mechanism to be easily integrated into a simulation.

The multi-step reaction model that includes various reaction paths provides the dynamic model which was an initial objective of this study. The models have been benchmarked against test data such as the ODTX scenarios. An example model was shown here that responds differently to the burning and detonation regime. Future work should be performed to validate a multi-step model that incorporates the multiple reaction paths.

9. References

- [1] T. Akenine-Möller, Fast 3D Triangle-box Overlap Testing, (2001).
- [2] Baer, M.R., Modeling heterogeneous energetic materials at the mesoscale. *Thermochimica Acta* **384** (1-2), 351-367 (2001).
- [3] Bdzil, J., Stewart, D., Modeling two-dimensional detonations with detonation shock dynamics. *Phys. Fluid A* **1** (7), 1261-1267 (1989).
- [4] Benson, D.J., An analysis by direct numerical simulation of the effects of particle morphology on the shock compaction of copper powder. *Modeling Simul. Mater. Sci. Eng.* **2** (3A) 535-550 (1994).
- [5] M. J. Berger and P. Colella, Local adaptive mesh refinement for shock hydrodynamics, *J. Comput. Phys.* **82**, 64-84 (1989).
- [6] M. J. Berger and R.J. LeVeque, *An Adaptive Cartesian Mesh Algorithm for the Euler Equations in Arbitrary Geometries*, AIAA Paper 89-1930-CP (1989).

- [7] M. J. Berger and J. Olier, Adaptive mesh refinement for hyperbolic partial differential equations, *J. Comput. Phys.* **53**, 484-512 (1984).
- [8] Chinnayya, A., Daniel, E., Saurel, R., Modelling detonation waves in heterogeneous energetic materials. *J. Comput. Phys.* **196**, 490-538 (2004).
- [9] Clifford, J.L., Milne, A.M., Turanyi, T., and Boulton, D., An Introduction Parameter Model for Shock-Induced Hydrogen Combustion Simulations. *The Journal of Combustion and Flame* **113** 106-118 (1998).
- [10] Clutter, J.K., *Computation of High-Speed Reacting Flows*, A Dissertation for the University of Florida, (1997).
- [11] Clutter, J.K., AFOSR Summer Fellowship Final Report.
- [12] Clutter, J.K., Belk, D., Simulation of detonation wave interaction using ignition and growth model. *Shock Waves* **12**, (3) 251-263 (2002).
- [13] J.K. Clutter, J. Mathis, and M. Stahl, Modeling environmental effects in the simulation of explosion events, *Int. J. Impact Eng.* **to appear**, (2006).
- [14] J.K. Clutter, M. Whitney, M. Stahl, and T. Slawson, *Design and Development of a Blast Load Simulator*, AIAA Paper 2001-0611 (2001).
- [15] Frey, R.B., Cavity collapse in energetic materials, *Proceedings of the 8th Symposium (Internationa) on Detonation* 68-80 (1985).
- [16] Hamate, Y., Horie, Y., Ignition and detonation of solid explosives: a micromechanical burn model. *Shock Waves* **16**, 125-147 (2006).
- [17] Johnson, J.N., Tang, P.K., Forest, C.A., Shock-wave initiation of heterogeneous reactive solids. *J. Appl. Phys.* **57** (9), 4323-4334 (1985).
- [18] Kang, J., Butler, P.b., Baer, M.R., A thermomechanical analysis of hot spot formation in condensed-phase, energetic materials. *Combust. Flame* **89** (117) (1992).
- [19] Kasimov, A., Stewart, D., Asymptotic theory of evolution and failure of self-sustained detonations. *J. Fluid Mech.* **525**, 161-192 (2005).
- [20] A.M. Khokhlov, Fully Threaded Tree Algorithms for Adaptive Refinement Fluid Dynamics Simulations, *J. Comput. Phys.* **143**, 519-543 (1998).

- [21] Kuo, K.K., *Principles of Combustion*, John Wiley & Sons, New York, NY, (1986).
- [22] Laney, Culbert B. *Computational Gasdynamics* Cambridge University Press (1998).
- [23] Lee, E.L., Tarver, C.M., Kasimov, A., Phenomenological model of shock initiation in heterogeneous explosives. *Phys. Fluids* **23** (12), 2362-2372 (1980).
- [24] LeVeque, R. J., Yee, H. C., A Study of Numerical Methods for Hyperbolic Conservation Laws with Stiff Source Terms. *J. Comput. Phys.* **86** 187-210 (1990).
- [25] Liou, Meng-Sing, A Sequel to AUSM: AUSM+. *J. Comput. Phys.* **129** 364-382 (1996).
- [26] Liou, M.-S., Steffen, C., A New Flux Splitting Scheme. *J. Comput. Phys.* **107** 23-39 (1993).
- [27] Maas, U. and Pope, S.B., Simplifying Chemical Kinetics: Intrinsic Low-Dimensional Manifolds in Composition Space. *The Journal of Combustion and Flame* **88** 239-264 (1992).
- [28] Massoni, J., Saurei, R., Baudin, G., Demol, G.. *Phys. Fluids* **11** (3), 710-736 (1999).
- [29] NIST Scientific and Technological Databases, NIST-JANAF Thermochemical Table, Fourth Edition. *Journal of Physical and Chemical Reference Data* (1998).
- [30] T. Ogawa, Development of a flow solver using the adaptive Cartesian mesh algorithm for wind environment assessment, *J. Wing Eng. Ind. Aerodyn.* **81**, 377-389 (1999).
- [31] Orkwis, P.D., and Vanden, K.J., *On the Accuracy of Numerical Versus Analytical Jacobians* AIAA Paper 84-0176 (1994).
- [32] Sandia National Laboratories, *Numerical Recipes in C: The Art of Scientific Computing*, Cambridge University Press, 43-50 (1992).
- [33] Shuen, J. S., Upwind Differencing and LU Factorization for Chemical Non-Equilibrium Navier-Stokes Equations. *J. Comput. Phys.* **99** 233-250 (1992).

- [34] Steger, J., Warming, R.F., Flux Vector Splitting of the Inviscid Gasdynamics Equations with Application to Finite-Difference Methods. *J. Comput. Phys.* **40** 263-293 (1981).
- [35] Strang, On the construction and comparison of difference schemes. *J. Numer. Anal.* **5**, 506 (1968).
- [36] Tarver, C.M., Chidester, S.K., On the Violence of High Explosive Reactions, *2004 ASME Pressure Vessels & Piping Conference* (2004).
- [37] Van Leer, B., Flux Vector Splitting for the Euler Equations. *Lecture Notes in Physics Volume 170, Eighth International Conference of Numerical Methods in Fluid Dynamics*, ed. E. Krause, Springer-Verlag. 507-512 (1982).
- [38] J. Wackers and B. Koren, *A Simple and Efficient Space-Time Adaptive Grid Technique for Unsteady Compressible Flows*, AIAA Paper 2003-3825 (2003).
- [39] Williamson, R.L., . *J. Appl. Phys.* **68** (3) (1990).
- [40] Yoh, J.J., McClelland, M.A., Maienschein, J.L., Wardell, J.F., Tarver, C.M., Simulating thermal explosion of cyclotrimethylenetrinitramine-based explosives: Model comparison with experiment. *J. Applied. Phys.* **97**, 083504 (2005).

DISTRIBUTION LIST
AFRL-RW-EG-TR-2007-7130

Defense Technical Information Center 1
Attn: Acquisition (OCA)
8725 John J. Kingman Road, Ste 0944
Ft Belvoir, VA 22060-6218

EGLIN AFB OFFICES:

AFRL/RW CA-N	1
AFRL/RWOC-1 (STINFO Office)	1
AFRL/RWA	1
AFRL/RWG	1
AFRL/RWM	1
AFRL/RWAC	1